Roozbeh (Ross) Salary
Department of Mechanical Engineering,
College of Engineering and Computer Sciences,
Marshall University,
Huntington, WV 25755;
Center for Advanced Microelectronics Manufacturing,
State University of New York at Binghamton,
Binghamton, NY 13902
e-mail: salary@marshall.edu

Jack P. Lombardi
Center for Advanced Microelectronics Manufacturing,
State University of New York at Binghamton,
Binghamton, NY 13902
e-mail: jlombar4@binghamton.edu

Darshana L. Weerawarne
Center for Advanced Microelectronics Manufacturing,
State University of New York at Binghamton,
Binghamton, NY 13902;
Department of Physics,
University of Colombo,
Colombo 00300, Sri Lanka
e-mail: dweeraw1@binghamton.edu

M. Samie Tootooni
Department of Health Informatics and Data Science,
Loyola University Chicago,
Maywood, IL 60153
e-mail: mtootoo1@binghamton.edu

Prahalada K. Rao
Department of Mechanical & Materials Engineering,
University of Nebraska–Lincoln,
Lincoln, NE 68588
e-mail: rao@unl.edu

Mark D. Poliks[1]
Center for Advanced Microelectronics Manufacturing,
State University of New York at Binghamton,
Binghamton, NY 13902
e-mail: mpoliks@binghamton.edu

A Sparse Representation Classification Approach for Near Real-Time, Physics-Based Functional Monitoring of Aerosol Jet-Fabricated Electronics

Aerosol jet printing (AJP) is a direct-write additive manufacturing (AM) method, emerging as the process of choice for the fabrication of a broad spectrum of electronics, such as sensors, transistors, and optoelectronic devices. However, AJP is a highly complex process, prone to intrinsic gradual drifts. Consequently, real-time process monitoring and control in AJP is a bourgeoning need. The goal of this work is to establish an integrated, smart platform for in situ and real-time monitoring of the functional properties of AJ-printed electronics. In pursuit of this goal, the objective is to forward a multiple-input, single-output (MISO) intelligent learning model—based on sparse representation classification (SRC)—to estimate the functional properties (e.g., resistance) in situ as well as in real-time. The aim is to classify the resistance of printed electronic traces (lines) as a function of AJP process parameters and the trace morphology characteristics (e.g., line width, thickness, and cross-sectional area (CSA)). To realize this objective, line morphology is captured using a series of images, acquired: (i) in situ via an integrated high-resolution imaging system and (ii) in real-time via the AJP standard process monitor camera. Utilizing image processing algorithms developed in-house, a wide range of 2D and 3D morphology features are extracted, constituting the primary source of data for the training, validation, and testing of the SRC model. The four-point probe method (also known as Kelvin sensing) is used to measure the resistance of the deposited traces and as a result, to define a priori class labels. The results of this study exhibited that using the presented approach, the resistance (and potentially, other functional properties) of printed electronics can be estimated both in situ and in real-time with an accuracy of $\geq 90\%$. [DOI: 10.1115/1.4047045]

Keywords: advanced manufacturing, aerosol jet printing (AJP), monitoring and control, sparse representation classification (SRC), artificial intelligence, flexible and hybrid electronics

1 Introduction

1.1 Objective and Motivation. The goal of this work is to establish an integrated, smart platform for real-time estimation and monitoring (and closed-loop control in the future) of the functional properties—including but not limited to electrical and mechanical properties, e.g., resistance, Young's modulus, hardness, and fatigue life—of aerosol jet-fabricated electronics. In pursuit of this goal, the objective of the work is to forward a multiple-input, single-output (MISO) intelligent learning model—established upon sparse representation classification (SRC)—to estimate the functional properties in situ and in near real-time. The aim is to classify the resistance of an aerosol jet (AJ)-printed electronic trace (line) into an a priori class as a function of consequential parameters of aerosol jet printing (AJP) process (i.e., sheath gas flowrate (ShGFR) and exhaust gas flowrate (EGFR) in addition to print speed) as well as a broad spectrum of the 2D and 3D morphological characteristics of the printed line (e.g., line width, thickness, and cross-sectional area (CSA)). To realize this objective, in situ and real-time images are acquired from the deposited line using a high-resolution charge-coupled device (CCD) camera and the AJP process monitor camera, respectively. Subsequently, the acquired images are analyzed using a range of digital image processing algorithms, developed in-house, allowing for rapid quantification of the morphological characteristics. These image-based, extracted characteristics constitute the primary source of data for the training, validation, and testing of the SRC model. A priori class labels are defined based on the resistance of a set of AJ-deposited lines, measured using the four-point probe method. The performance of the SRC model is assessed not only by performing a large number of

[1]Corresponding author.

Manuscript received November 20, 2018; final manuscript received April 10, 2020; published online May 18, 2020. Assoc. Editor: Qiang Huang.

simulations (with random data partitioning) and then observing several performance measures, e.g., F-Score, but also by contrasting the SRC model's performance with that of several well-known classifiers, such as artificial neural network (ANN), k-nearest neighbors (kNN, support vector machine (SVM), and ensemble of learners.

A direct-write additive manufacturing (AM) technique [1], AJP, has been extensively used for the fabrication of a broad spectrum of electronics, such as transistors [2–4], fine-pitch electronics [5], sensors [6,7], organic light emitting diodes [8], and optoelectronic devices [9]. This is, to a great extent, due to the unique capabilities and advantages of AJP, including (i) deposition of fine microstructures with feature sizes as small as 10 μm; (ii) accommodation of a wide range of ink viscosity, ranging from 0.7 to 2500 cP; and (iii) having a variable, large standoff distance, which allows for material deposition on nonplaner surfaces [1,10,11]. Note that the printing resolution of other direct-write AM techniques (such as inkjet printing and dispensing printing) does not reach that of AJP. This is because AJP utilizes a sheath gas flow, which collimates the aerosol flow prior to deposition. Furthermore, the pneumatic atomizer of AJP, working based on a high-pressure flow of an inert gas, is capable of atomization of inks with high viscosity; such an aerodynamic characteristic is not embedded in other direct-write AM techniques. Figure 1 exemplifies electronic devices, AJ-fabricated at State University of New York (SUNY) at Binghamton.

Despite the aforementioned advantages and host of critical applications, AJP is intrinsically complex [12], prone to gradual drifts and changes in machine behavior and deposited material. The gradual drifts in AJP result from dynamic phenomena in the process, e.g., changes in ink viscosity (due to solvent evaporation and/or an increase in ink temperature) as well as accumulation of ink in the aerosol transport tube. Such gradual changes in AJP lead to process drift characterized, for example, by an increase in the rate of material deposition, insufficient aerosol flow density, and nozzle clog. All in all, the presence of inevitable process drift in AJP results in deviation of both geometrical and electrical properties from their set design tolerances. Therefore, real-time process monitoring and control is a burgeoning need.

As illustrated in Fig. 2, the authors' prior works [13–15,17] paved the way for implementation of image-based monitoring and control of the functional properties of electronics in AJP process by introducing a broad range of image processing algorithms (allowing for in situ quantification of the morphology) as well as closed-loop control methods [18]. The purpose of this work is to bridge the gap between image-based sensor data and process monitoring/control by forwarding an intelligent learning model to estimate, monitor, and ultimately control the functional properties of AJ-fabricated electronics.

Resistance is an important functional property of electronics. If the resistance of a printed electronic (or a component) exceeds its design tolerances, it is considered defective. Traditionally, line resistance measurements are carried out offline using, e.g., the four-point probe method. It would be challenging to measure line resistance directly in situ, since the probe needles must physically be placed on unsintered, wet printed lines. Hence, in situ estimation of line resistance allows for real-time monitoring of the functional integrity of electronics and, in case of a drift, control (correction) of the AJP process. This ensures continuous fabrication of conformal electronics and reduces the amount of scrap and rework. Note that this study focuses on conductive inks.

The following challenges are intrinsically associated with the proposed method for real-time estimation and monitoring of the functional properties of AJ-printed electronics. First, image acquisition should be performed at high frame rates; this allows for faster detection of anomalies and process drift. Second, the image processing algorithms, utilized to analyze the acquired images to extract the morphological traits of the printed electronics, should be computationally fast. Image windowing and development of image processing algorithms in, for example, PYTHON or C++ could remarkably lessen the delay stemming from image processing. Third, the classification algorithms used for the estimation of the functional properties should be similarly fast as well as robust over a range of class labels; we will demonstrate in Sec. 3.2 that, for example, ANN fails to classify line resistance when the number of a priori class labels is greater than six. Furthermore, the classification algorithms should be able to handle nonstationary and nonlinear data and/or data with autocorrelation, intermittency, periodicity, and low signal-to-noise ratio; this is unavoidable because monitoring of AJP process interracially entails complex multivariate sensor data.

Overall, the outcomes of this work allow for dissemination of knowledge concerning the performance of the SRC classifier, particularly in the area of additive manufacturing. Besides, it enables AJP users to monitor the functional properties of AJ-fabricated electronics in near real-time. Finally, this work pays the way for implementation of closed-loop control of printed electronics' functional properties in the future.

1.2 Aerosol Jet Printing Process. Figure 3 illustrates the AJP process, utilizing a pneumatic atomizer (PA) as the mechanism of choice for aerosol generation. A high-pressure flow of an inert gas—typically pure and dry N_2 referred to as atomization gas flow (AGF)—is injected into the ink reservoir via a constricted tube positioned over a capillary. Based on the Venturi effect, the ink is drawn upward in the capillary and then sheared by the atomization jet passing through an orifice; consequently, a fine spray of micro-droplets is generated. Larger droplets fall back into the reservoir, while smaller ones form a semi-uniform multiphase flow toward the virtual impactor.

Depending on the ink of choice, the bubbler is filled with the ink solvent/co-solvent, which provides a saturated flow prior to atomization, and thus minimizes the loss of solvent due to evaporation

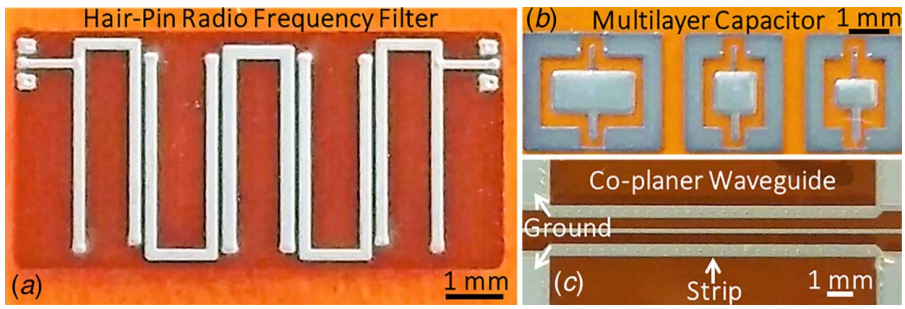

Fig. 1 Examples of electronic devices, AJ-fabricated at SUNY-Binghamton. (*a*) A silver nanoparticle-based hair-pin radio frequency filter, printed on Kapton. (*b*) Multilayer capacitors, composed of silver nanoparticle and dielectric inks (layer arrangement: conductor, dielectric, conductor). (*c*) A 1-in. long co-planer waveguide structure, made of silver nanoparticles on Kapton; the ground lines are connected to a conductor layer via holes.

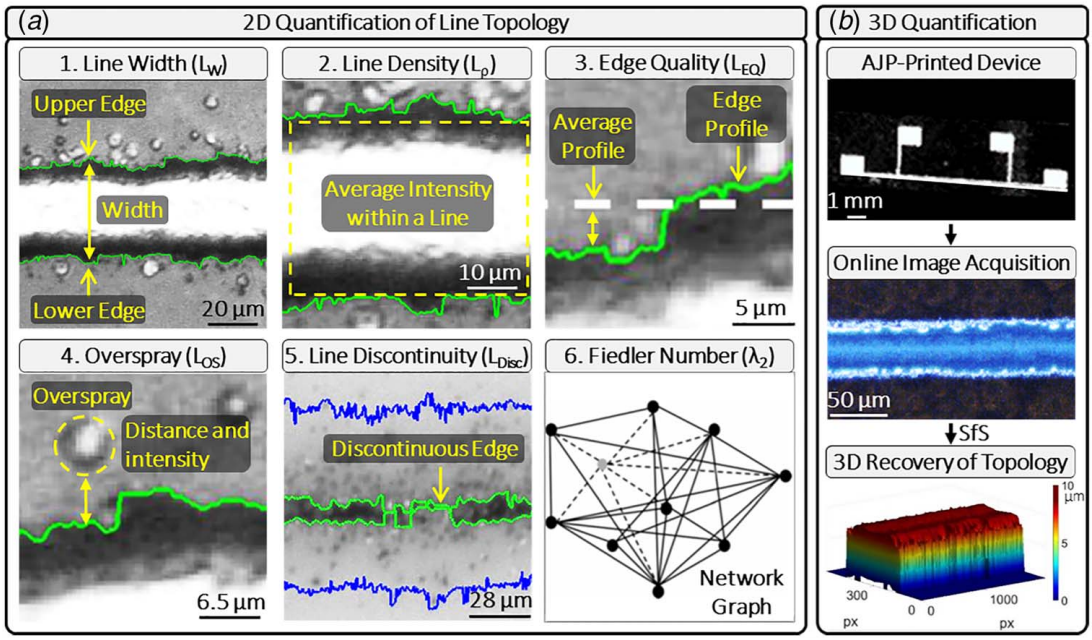

Fig. 2 The concept behind the image processing algorithms used for in situ and real-time quantification of the morphology characteristics of printed electronics. The quantified traits together with AJP process parameters are fed as input features for the estimation of the functional properties using the SRC intelligent model (Source: Refs. [13–16]). (*a*) 2D quantification of line topology and (*b*) 3D quantification.

from the ink (otherwise causing the ink viscosity to change). This process of saturating the atomization gas utilizes a sparger, allowing for an efficient gas–liquid contact. Wadhwa [19] studied the rate of solvent loss from a co-solvent solution system as well as the rate of solvent added back to the atomization gas flow when passed through the bubbler. They demonstrated that adding solvent(s) to the atomization gas flow would be an effective method to overcome the loss of solvent (i.e., one of the root-causes of process drift in AJP). They also illustrated that the loss of solvent due to evaporation is a nonlinear function of temperature.

The virtual impactor aerodynamically separates the droplets that have relatively low linear momentum and small size using an exhaust gas flow (EGF), while allowing the rest to flow as a uniform stream of aerosols toward the deposition head. In the deposition head, a second gas flow, called the sheath gas flow (ShGF), is concentrically introduced to collimate the aerosol flow into a narrow beam. The rate ratio of the ShGF to the aerosol flow is termed the *focusing ratio* [20]. The collimated aerosol flow ultimately accelerates (while its pressure decreases) passing through a fine, converging nozzle (made up of ceramic), and impinges on a free surface. The aerosols additively constitute a free-form structure, having experienced post-deposition phenomena of spreading, receding, relaxation, and coalescence [21].

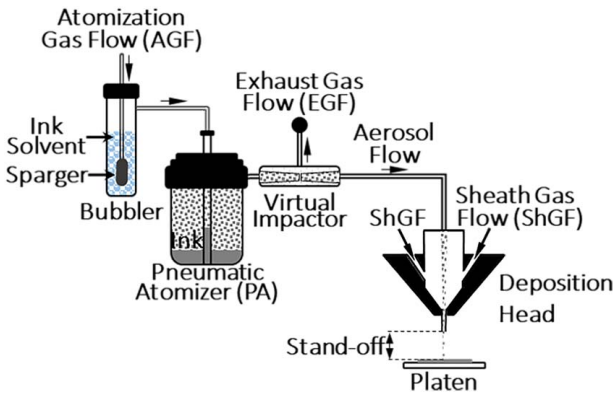

Fig. 3 A schematic flow diagram of the aerosol jet printing process. In this configuration, pneumatic atomization is the mechanism of choice for aerosol generation. A uniform and collimated flow of aerosols is obtained with the aid of the virtual impactor and the deposition head, respectively.

1.3 Sensor-Instrumented Setup

1.3.1 In Situ Monitoring Using a CCD Camera. As illustrated in Fig. 4, an Optomec AJ-300 aerosol jet printer (Albuquerque, NM) was instrumented with a high-resolution (5 MP) CCD camera (Edmund Optics, Grasshopper, GS3-U3-50S5C-C, Barrington, NJ), allowing for independent, in situ image acquisition. The images acquired by this camera have a maximum window size of 2448×2048 pixels. Co-axial to the nozzle, the camera was mounted on a 2.5 × –10 × variable magnification lens (Edmund Optics, VZM 1000i, Barrington, NJ). The resolution of the imaging system is approximately 0.36×0.36 μm/pixel in the x- and y-directions, respectively. Illumination was provided by an light-emitting diode (LED) light (AmScope, Irvine, CA); it has a maximum brightness of 30,000–40,000 Lux and a color temperature of 6000 K. Note that in this study, the term "in situ" is used to refer to in-process or on-demand process monitoring, while the term "real-time" is used to refer to instantaneous process monitoring.

1.3.2 Real-time Monitoring Using the Process Monitor Camera. Positioned inclined to the platen at about 45 deg, the AJP process monitor camera is a 1.3 MP GigE color camera (Point Grey Flea3, Richmond, BC, Canada), mounted on an optical 1.0× lens as well as a 4.0× magnification module (Infinity Photo-Optical InfiniStix™, Boulder, CO). The lens has a working distance of 94 mm. Illumination for this camera was provided by a fiber light (Dolan-Jenner PL-800, Boxborough, MA), mounted opposite to the camera. The illumination position was adjusted such that noise-free, saturated background images were obtained, aiding in accurate detection of line edges (for example, see Fig. 13). Being of *raw12* data format, the images acquired by the process monitor camera were saved as *.tif* file format.

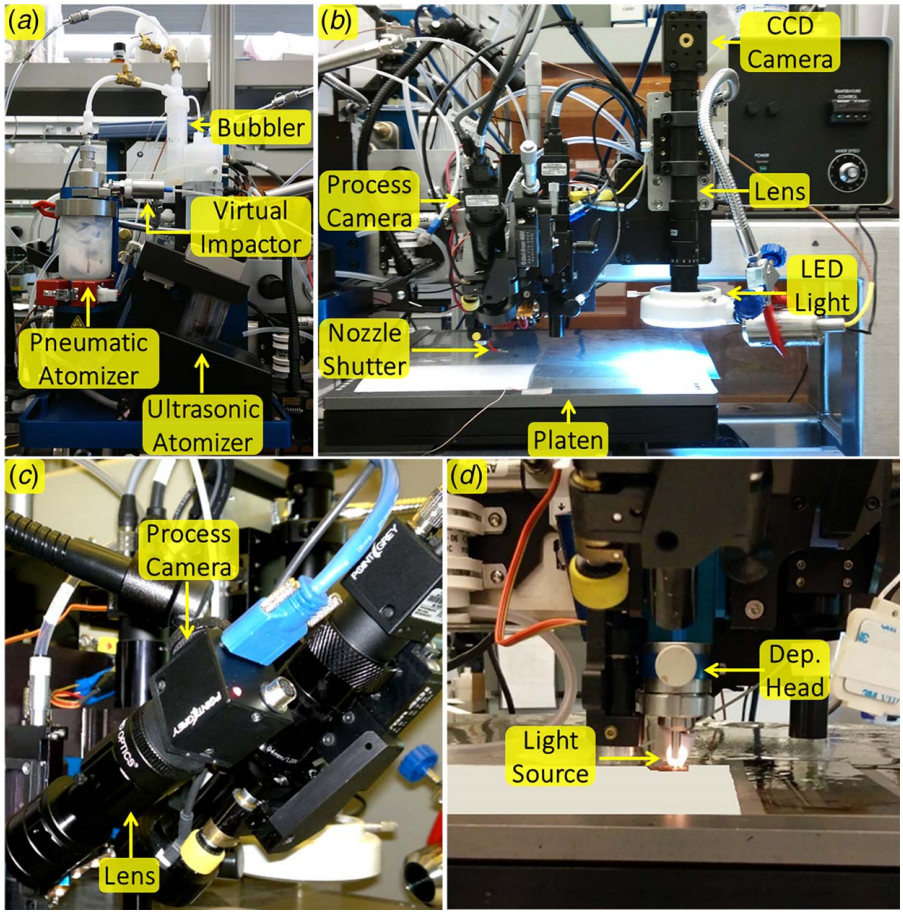

Fig. 4 Pictures of the AJP experimental setup, instrumented with a high-resolution CCD camera mounted on a variable magnification lens, allowing for in situ image acquisition. In addition, the standard process monitor camera is used for real-time image acquisition.

The rest of the paper is presented as follows: Sec. 2 details the development of the SRC intelligent learning model, including mathematical formulation as well as numerical implementation. In situ and real-time experimental results—consisting of: (i) materials, (ii) design of experiments, (iii) observations, and (iv) model assessment—is delineated in Sec. 3. The conclusions and future works are presented in Sec. 4.

2 Development of an Intelligent Learning Model

In this section, the development of a new supervised learning model (based on SRC) is delineated. Generally, the aim of supervised learning—where there exists prior knowledge (history) about the output values of a machine or a process—is to approximate an input–output mapping function, capable of estimating the future output values of the process correspondingly versus input data. Similarly, in this study, the forwarded SRC model is used with the aim to estimate the resistance (and potentially, other functional properties as output variables) of printed electronics, as a function of input variables, i.e., (i) image-based data streams of the morphology and (ii) AJP process parameters. This requires real-time characterization of the morphology as well as extraction of morphology features. Hence, the SRC classifier is trained based on the history of the AJP process, relating morphology features (e.g., line width, thickness, and cross-sectional area) in addition to influential process parameters (e.g., ShGFR, EGFR, and print speed (PS)) to resistance. Once trained and validated, the classifier is capable of estimating and monitoring the resistance of electronics, fabricated in situ (see Sec. 3.2) and in real-time (see Sec. 3.3).

Artificial intelligence and deep learning have been extensively utilized in a broad range of manufacturing applications. Kothuru et al. [22] proposed an intelligent monitoring method, based on SVM and convolutional neural network, with the aim to detect and predict milling tool condition (particularly, cutting tool wear) in machining of parts with hardness variation. Similarly, Wu et al. [23] developed a cloud-based, parallel random forests (RF) learning algorithm (capable of training large-scale predictive models) for prediction of milling tool wear. The forwarded method demonstrated a significant reduction in computation time, while maintaining a high prediction accuracy. In a research work by Khanzadeh et al. [24], unsupervised self-organizing map (SOM) machine learning approach was used to characterize the dimensional accuracy of complex geometries, fabricated using fused filament fabrication process, on the basis of laser-scan point cloud data. The presented SOM-based method was swift, requiring less than 3% of over one million data points for the characterization of part dimensional accuracy. A combined, decision tree (DT)-based ensemble learning approach—composed of RF, gradient boosting trees, as well as extremely randomized trees algorithms—was developed by Li et al. [25] for accurate prediction of material removal rate in chemical mechanical planarization (CMP) process with the aim to achieve uniform surface finish. Du et al. [26] presented a novel sparse learning model (together with a parameter estimation algorithm), with the goal to optimally place actuators for shape adjustments in fuselage assembly process. With the aid of a multimodal, deep-learning approach, He and Jin [27] established a framework for prediction of failure mechanisms, estimation of remaining life, and ultimately real-time monitoring of ion mill etching process. The presented approach was

based on RF classification in addition to long short-term memory (LSTM), an artificial recurrent neural network architecture. Imani et al. [28] introduced a computationally fast, machine learning approach—established based upon a deep neural network, capable of learning image-captured layerwise variant geometry—to accurately detect fine flaws in additive fabrication of complex parts. Utilizing shape-to-image registration, the proposed approach proved to be efficient for interlayer variation reduction and thus in situ correction of additive manufacturing processes. In a study by Han et al. [29], an enhanced iterative learning method (also known as iterative learning control) was used to optimize drilling depth in deep hole drilling process (with an accuracy of >90%). The presented iterative leaning method would further allow for prediction of both drill life and machining efficiency.

The SRC [30,31] has emerged as an accurate and computationally fast supervised classification approach [32,33] and been utilized in a broad range of applications, such as computer vision [34], healthcare [35], damage detection [36], and real-time monitoring of advanced manufacturing processes [33]. Using the SRC, Tootooni et al. demonstrated: (i) classification of global neurophysiological states from electroencephalography signals [37] and (ii) classification of the dimensional variation of additively manufactured parts [38]. In addition, they showed that the SRC could be successfully implemented for classification of nonstationary and nonlinear data, similar to the AJP image-based sensor data, discussed in this study [37]. Furthermore, it has been demonstrated that the SRC can handle data with autocorrelation, intermittency, periodicity, and low signal-to-noise ratio [37,39,40].

Table 1 summarizes the main characteristics of several well-known classifiers, including ANN, DT, discernment analysis (DA), Naïve Bayes (NB), kNN, SVM, and ensemble of learners (Ens), compared with some of the important characteristics of the SRC classifier. It turns out that the SRC is a potentially suitable and flexible classifier for in situ functional monitoring of AJ-printed electronics that inherently comprises complex multivariate sensor data. This hypothesis is experimentally tested in this study.

2.1 Sparse Representation Classification. There are several SRC methods, reviewed in detail in Refs. [32,33]. The SRC has been established, based on the fact that the sensor data streams that belong to the same thermodynamic state of an open system (such as AJP) under steady-state conditions, have stronger correlation than the data streams that are collected from different thermodynamic states of the system. The SRC formulates a supervised classification problem as an underdetermined system of linear equations [31,32] where the input vector of classification features, $\boldsymbol{Y} \in \mathbb{R}^{m\times 1}$, is expressed as a linear combination of design data, $\mathbf{A} \in \mathbb{R}^{m\times N}$, which reflects the history of a process, as mathematically expressed by Eq. (1), where N stands for the total number of already-collected samples and m stands for the total number of classification features; in addition, ε represents the approximation error [30,32]

$$\boldsymbol{Y} = \mathbf{A}\boldsymbol{\beta} + \varepsilon \tag{1}$$

In this study, the input vector of classification features ($\boldsymbol{Y}$), which contains image-based morphology traits as well as AJP process parameters. The function of $\boldsymbol{Y}$ is twofold: (i) regarding model validation and testing, it contains already-collected values of the classification features; (ii) regarding process monitoring, it is composed of instantaneously collected (dynamic) values of the classification features. Note that in the latter case, $\boldsymbol{Y}$ reflects the most recent morphology of an electronic being fabricated.

Table 1 A review of the main characteristics of several machine learning algorithms, whose performance is contrasted against that of the forwarded SRC method in this study for in situ as well as near real-time estimation of the functional properties of AJ-fabricated electronics

Method	Abb.	Characteristics
Sparse representation classification	SRC	• Accurate and computationally fast [32,33]; • Handles nonstationary and nonlinear data as well as data with autocorrelation, intermittency, periodicity, and low signal-to-noise ratio [37,39,40].
Artificial neural network	ANN	• Detects complex relationships between multiple-inputs and multiple-outputs [41]; • Has limited ability to identify causal relationships [41]; • Prone to overfitting [41]; • Has relatively medium accuracy, medium computation speed, and medium computation difficulty [42]; • Sensitive to sample size, nonlinearity, high correlation, unequal covariance, in addition to multimodal distribution [43].
Decision tree	DT	• Efficient and accurate, compared with conventional single-stage classification algorithms [44]; • Sensitive to noise in training data [45]; • Computationally fast learning [45]; • Supports incremental learning [46]; • Prone to overfitting [46];
Discernment analysis	DA	• Sensitive to non-normality and high correlation [43]; • Insensitive to unequal sample proportion [43].
Naïve Bayes	NB	• Requires short computation time for training [46]; • Progressively enhances performance via removing insignificant classification features [46]; • Requires a large number of samples for proper training [46].
k-Nearest neighbors	kNN	• Sensitive to sample size, unequal covariance, and multimodal distribution [43]; • Computationally fast learning [46]; • Insensitive to noise in training data as well as class size [46].
Support vector machine	SVM	• A semi-parametric (kernel function-based) method [47]; • Assumes that a priori class labels are linearly separable [47]; • High prediction accuracy vis-à-vis computation speed [42]; • Medium computation speed and difficulty [42].
Ensemble of learners	Ens	• High prediction accuracy and stability [42]; • Low computation speed [42]; • High computation difficulty [42].

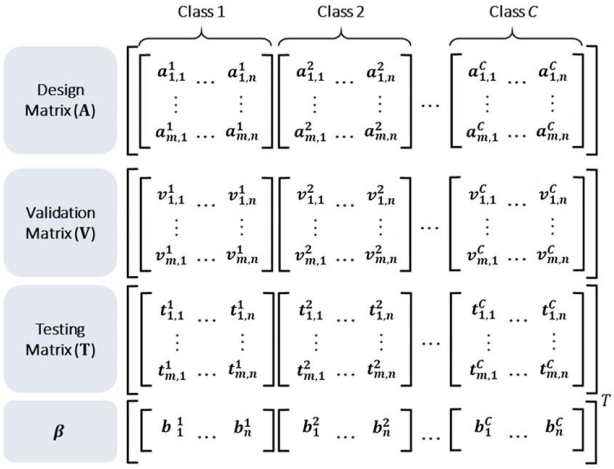

Fig. 5 The structure of the design (A), validation (V), and testing (T) matrices as well as of the vector of membership coefficients (β). Each matrix/vector is a concatenation of submatrices/subvectors over all class labels. Classification features are placed in the rows and individual observations (samples) in the columns.

Known as the measurement matrix, the design matrix ($\mathbf{A}$) relates the classification features to line resistance, as follows. In this study, it reflects the history, i.e., the previous thermodynamic states, of the AJP process. Envisioned in Fig. 5, the design matrix takes the following form: $\mathbf{A} = [\mathbf{A}^1_{m,n}\ \mathbf{A}^2_{m,n} \ldots\ \mathbf{A}^C_{m,n}]$, where $C \in \{1, 2, 3, \ldots\}$ represents a priori classification labels. In this work, they were defined based on four-point probe measurements (as discussed in Secs. 3.2.3 and 3.3.3). Note that in the expanded form of the design matrix, the classification features (listed in Table 2) are placed in the rows ($i = 1 \ldots m$), and individual observations or samples per class (i.e., acquired individual images and/or segmented parts of them) are placed in the columns ($j = 1 \ldots n$). The total number of samples (N) is expressed as $N = n \times C$.

As categorized in Table 2, the classification features include (i) three AJP process parameters; (ii) 2D and 3D quantified characteristics (traits) of line morphology, as discussed in detail in the authors' prior publications [13–15,17]; (iii) the first and last few graph-theoretic Laplacian eigenvalues [16]; and (iv) image-based texture measures [48]. Note that the texture measures are all statistical features, directly extracted from an image.

The 2D line morphology characteristics are based on pixel intensity gradients [13,14]. As depicted in Fig. 2, line width (L_W) represents the average distance between the detected edges of the line; line density (L_ρ) is defined as the average intensity of all the pixels forming the surface of the line; edge quality (L_{EQ}) is the reciprocal of the average distance between each edge and the mean line fitted through the edge; overspray (L_{OS}) is computed as the product of the intensity of a pixel and its distance from a line edge (averaged over the entire overspray space); line discontinuity (L_{Disc}) is defined as the average number of instances where no edge is detected.

Table 2 Input classification features, fed to the SRC model for the in situ and real-time estimation of line resistance, which are delineated in Refs. [13–17,48]

	Feature type	Component
1	Process parameter	ShGFR, PS, and EGFR.
2	2D characteristics of line morphology	L_W, L_ρ, L_{EQ}, L_{OS}, and L_{Disc}.
3	3D characteristics of line morphology	L_T and L_{CSA}.
4	Spectral graph-theoretic Laplacian eigenvalues	$\lambda_2{:}\lambda_6{\_}\lambda_{\text{end-4}}{:}\lambda_{\text{end}}$.
5	Texture measures (image histogram)	Mean, standard deviation, smoothness, skewness, uniformity, and entropy.
6	Texture measures (relative position)	Contrast, correlation, energy, homogeneity, and max probability.

Demonstrated in Fig. 2, the 3D characterization of line morphology is based on the concept of shape-from-shading (SfS). The 3D profile of a printed electronic can be reconstructed based on an image, illumination direction, as well as surface reflectivity. Once the 3D profile has been recovered, 3D morphology traits, such as line thickness (L_T), cross-sectional area (L_{CSA}), and surface roughness, are quantified.

The images—acquired for the in situ and real-time monitoring of line resistance, discussed in Secs. 3.2 and 3.3, respectively—are additionally transformed into an undirected and unweighted network graph [16,38], and subsequently, the first and last few graph-theoretic Laplacian eigenvalues (i.e., $\lambda_2{:}\lambda_6{\_}\lambda_{\text{end-4}}{:}\lambda_{\text{end}}$) are extracted from the resulting graph. As delineated in Ref. [38], the extraction of the eigenvalues involves: (i) calculation of the node degree of the graph; (ii) formation of a degree vector and transformation of the vector into a diagonal (degree) matrix; and (iii) formation of the Laplacian matrix, based on which the eigenvalues are extracted. In general, the Laplacian eigenvalues reflect various aspects of the algebraic connectivity of the graph. Tootooni et al. [37] showed that the eigenvalues could capture a significant portion of the variability of sensor data in complex systems.

Subsequent to the formulation of the classification problem as an underdetermined system of linear equations, mathematically expressed by Eq. (1), the unknown vector of membership coefficients, $\boldsymbol{\beta} \in \mathbb{R}^{N\times 1}$, needs to be estimated. Equation (1) implies that if $\boldsymbol{\beta}$ is known, the product of $\mathbf{A}\boldsymbol{\beta} \in \mathbb{R}^{m\times 1}$ estimates, with a certain error (ε), the values of the classification features (stored in $\boldsymbol{Y}$, obtained from instantaneous image acquisition). Following Fig. 5, note that the elements of $\boldsymbol{\beta}$ are associated with a priori class labels. Since the classification problem is ill-posed (i.e., the number of classification features is significantly less than the total number of samples, $m \ll N$), the classification problem, expressed by Eq. (1), is converted to a minimization problem as shown in Eq. (2), assuming $\boldsymbol{\beta}$ is sparse (meaning it has the smallest number of nonzero elements [32])

$$\begin{cases} \min \|\boldsymbol{\beta}\|_0 \\ \text{s.t.: } f(\boldsymbol{Y} - \mathbf{A}\boldsymbol{\beta}) \le \delta \end{cases} \tag{2}$$

where $\|\boldsymbol{\beta}\|_0$ represents the ℓ_0-norm (i.e., the number) of the unknown vector of membership coefficients to be minimized subject to a function of the fit/residual error, $\boldsymbol{Y} - \mathbf{A}\boldsymbol{\beta}$, being less than or equal to a set threshold (δ) [32]. In other words, as represented by Eq. (2), $\boldsymbol{\beta}$ is estimated with a minimum number of elements that collectively result in a residual error, enforced to be less than or equal to the threshold.

There are several works in the literature, dedicated to the direct solving of the sparse estimation problem represented by Eq. (2), which is inherently an non-deterministic polynomial-time (NP)-hard minimization problem [49–51]. Besides, there are categories of methods [32,33], which can be utilized to indirectly solve the aforementioned sparse estimation problem, including: (i) ℓ_1--minimization or convex optimization methods [52–55]; (ii) greedy methods [56–58]; and (iii) Bayesian methods [59–61]. The ℓ_1--minimization methods convert the sparse estimation problem to a convex optimization one, as mathematically expressed in Eq. (3) [32]

$$\begin{cases} \min \|\boldsymbol{\beta}\|_1 \\ \text{s.t.: } \|\boldsymbol{Y} - \mathbf{A}\boldsymbol{\beta}\|_2^2 \le \delta \end{cases} \tag{3}$$

In Eq. (3), $\|\boldsymbol{\beta}\|_1$ and $\|\boldsymbol{Y} - \mathbf{A}\boldsymbol{\beta}\|_2^2$, respectively, represent the ℓ_1-norm (i.e., the sum of absolute difference) of the unknown vector of membership coefficients, and the ℓ_2-norm (i.e., the sum of squared errors) of the fit error.

The least absolute shrinkage and selection operator (LASSO) [55] is an optimization method, which can be implemented based

on the shooting algorithm [62], the coordinate descent algorithm [63], and/or that of alternating direction method of multipliers (ADMM) [64], among others. The ADMM was used as the algorithm of choice in this work. Note that total variation regularization [54], Dantzig selector [52], and basis pursuit de-noising [53], are other convex optimization methods that can be used to solve the sparse estimation problem indirectly.

The second category of methods, i.e., the heuristic (greedy) methods—such as thresholding [58], regularized and stage-wise orthogonal matching pursuit (OMP) [56,58], subspace pursuit [65], least angle regression [57], and compressive sampling matching pursuit [66]—are relatively less computationally expensive. However, they may fail to reach the global minimum. Similar to the optimization methods, the greedy methods use the ℓ_2-norm of the fit error, i.e., $\|\boldsymbol{Y} - \mathbf{A}\boldsymbol{\beta}\|_2^2$ [32].

The third category of methods, i.e., the Bayesian methods, enforce sparsity, assuming a posterior distribution or a Gaussian likelihood function on the unknown vector of membership coefficients ($\boldsymbol{\beta}$) [32,33]; they are unlike the convex optimization methods or the greedy methods that provide point estimates of $\boldsymbol{\beta}$. Relevance vector machine (RVM) [59,60] as well as sparse Bayesian learning [61] are examples of the Bayesian methods.

Bastani et al. [33] proposed a combined greedy-Bayesian sparse estimation approach, utilizing the advantages of RVM (a Bayesian method) and OMP (a greedy method). Furthermore, they forwarded a spatially correlated Bayesian learning algorithm [67]—established based on RVM—for fault diagnosis (i.e., identification of dimensional variation) and ultimately, part dimensional integrity in multistation assembly systems (in the inevitable presence of spatial correlation among process errors). Barazandeh et al. [32] developed a robust, hybrid SRC algorithm, capable of classifying sensor data in the presence of outliers and non-Gaussian noises.

In this study, the convex optimization formulation, expressed by Eq. (3), was expanded into a new combined form, demonstrated by Eq. (4), with incorporation of not only

(i) the sum of squared errors of estimation, i.e., the ℓ_2-norm of the fit error, $\|\boldsymbol{Y} - \mathbf{A}\boldsymbol{\beta}\|_2^2$, and
(ii) the sum of absolute difference, i.e., the ℓ_1-norm, of the vector of membership coefficients, $\boldsymbol{\beta}_1$, but also
(iii) the ℓ_2-norm, of the vector of membership coefficients, $\|\boldsymbol{\beta}\|_2^2$

$$\begin{cases} \min\left(\dfrac{1-\alpha}{2}\|\boldsymbol{\beta}\|_2^2 + \alpha\|\boldsymbol{\beta}\|_1\right) & \text{for } 0 < \alpha \le 1 \\ \text{s.t.: } \|\boldsymbol{Y} - \mathbf{A}\boldsymbol{\beta}\|_2^2 \le \delta \end{cases} \tag{4}$$

The sparse estimation-based classification is a twofold approach:

(i) The first step is to estimate the unknown vector of membership coefficients ($\boldsymbol{\beta}$) as mathematically expressed by Eq. (5). In this study, the estimation of $\boldsymbol{\beta}$ was carried out using a combination of the LASSO [55], elastic net (EN) [68], and ridge regression (RR) [69].
(ii) The second step is to determine the class label, i.e., the resistance range (in this study), of dynamically captured input sets of the classification features (stored in $\boldsymbol{Y}$) as mathematically expressed by Eq. (6). As discussed, the classification features reflect not only the most recent morphology of a printed electronic but also AJP process conditions

$$\hat{\beta} = \underset{\beta}{\operatorname{argmin}}\left(\begin{array}{c} \|\boldsymbol{Y} - \mathbf{A}\boldsymbol{\beta}\|_2^2 \\ + \lambda\left(\dfrac{1-\alpha}{2}\|\boldsymbol{\beta}\|_2^2 + \alpha\|\boldsymbol{\beta}\|_1\right) \end{array}\right) \tag{5}$$

In Eq. (5), $\lambda \in \mathbb{R}$ is a regularization parameter, which controls the overall contribution of the penalty term $\left(\frac{1-\alpha}{2}\|\boldsymbol{\beta}\|_2^2 + \alpha\|\boldsymbol{\beta}\|_1\right)$. The $\hat{\boldsymbol{\beta}} \in \mathbb{R}^{N\times 1}$, i.e., the estimated vector of membership coefficients, has been concatenated over all class labels, defined as $\hat{\boldsymbol{\beta}}_{N,1} \underline{\underline{\text{def}}} [\hat{\boldsymbol{\beta}}_{n,1}^{1\,T}\ \hat{\boldsymbol{\beta}}_{n,1}^{2\,T} \ldots \hat{\boldsymbol{\beta}}_{n,1}^{C\,T}]^T$. $\alpha \in \mathbb{R}$ is a weighting parameter, being between (0 1]; if $\alpha \approx 0$, the problem is formulated based on ridge regression; if $\alpha = 1$, the problem is formulated based on the LASSO; and if $0 < \alpha < 1$, it is based on elastic net.

Finally, as indicated by Eq. (6), the class label of an input vector ($\boldsymbol{Y}$) of the classification features is estimated to be $\hat{C} \in \{1, 2, 3, \ldots\}$, if the corresponding membership coefficients of that class, i.e., $\hat{\boldsymbol{\beta}}^{\hat{C}} \in \mathbb{R}^{n\times 1}$, yield the minimum of the fit error among other class labels. In Eq. (6), $\delta_c(\hat{\boldsymbol{\beta}})$ is an operator which creates a sparse vector of $\hat{\boldsymbol{\beta}}$ where all elements (coefficients) are zero except those of class c for $c = 1, 2, \ldots, C$; in other words, $\delta_c(\hat{\boldsymbol{\beta}}) = [0 \ldots \hat{\boldsymbol{\beta}}_{n,1}^{c\,T} \ldots 0]^T$

$$\hat{C} = \underset{c}{\operatorname{argmin}}\,(\mathbf{A}\delta_c(\hat{\boldsymbol{\beta}}) - \boldsymbol{Y}) \text{ for } c = 1, 2, \ldots, C \tag{6}$$

2.2 Numerical Implementation. Figure 6 illustrates a pseudocode for the numerical implantation of the proposed SRC model. It comprises four steps: (i) initialization; (ii) data preparation; (iii) validation (parameter optimization); and (iv) testing. The last two steps run a common classification subroutine.

2.2.1 Initialization. The results of in situ and real-time image processing and quantification of line morphology are stored in a matrix, called the *Grand Matrix*, where the quantified morphology traits along with AJP process parameters (which together form classification features) are placed in the rows and individual samples/observations in the columns. Depending on the trade-off between the depth of learning versus computation time, a combination of the classification features is selected and stored in a new matrix (called the *Feature Matrix*). This matrix is used as the primary source of data. Partitioning percentages are specified accordingly for the training, validation, and testing of the model. Corresponding to the number of samples, a vector of a priori class labels is defined; the range of each class is based on the objectives as well as the resolution of process monitoring. Two ranges of values are defined for both the regularization parameter (λ) and the weighting parameter (α), as well.

2.2.2 Data Preparation. The SRC model requires allocation of an equal number of samples to each class. Therefore, if n^C is the number of samples in class C where $\in\{1, 2, 3, \ldots\}$, the overall number of samples picked by the *Data Preparation* algorithm is: $\min(n^1, n^2, \ldots, n^C)$. Subsequently, according to the partitioning percentages (defined in step I), the training ($\mathbf{A}$), validation ($\mathbf{V}$), and testing ($\mathbf{T}$) matrices are randomly constructed (and then normalized) out of the feature matrix (as visualized in Fig. 5).

2.2.3 Validation (Parameter Optimization/Tuning). In this step, the optimum values of λ and α are estimated, based on the two ranges of values already defined in step I for these two parameters. The parameter optimization is implemented using a grid spacing (heuristic) approach, in which a 2D grid space is formed (established upon the number of divisions of the ranges defined for λ and α); subsequently, the performance of the *Classification Subroutine* is assessed at each grid point, employing the design ($\mathbf{A}$) and validation ($\mathbf{V}$) matrices. Once estimated, the optimal values of the regularization and weighting parameters (i.e., λ_{opt} and α_{opt}) are used, afterward, to classify the testing dataset ($\mathbf{T}$).

Note that the range of the classification parameters (i.e., the grid dimensions) should be broad enough to ensure reaching the global optimum; this results in an increase in the processing time. In addition, the grid spacing influences not only the accuracy of the validation process—the smaller the grid spacing, the more accurate the parameter estimation—but also the processing time. As a result, an optimal combination of the grid dimensions and spacing should be adopted to obtain an efficient estimation of the classification parameters (see Fig. 11 in Sec. 3.2.3 as an example, demonstrating the parameter estimation process).

2.2.4 Testing. For the model testing, the classification subroutine is executed to independently assess the performance of the trained model, using the untouched matrix of testing ($\mathbf{T}$). The

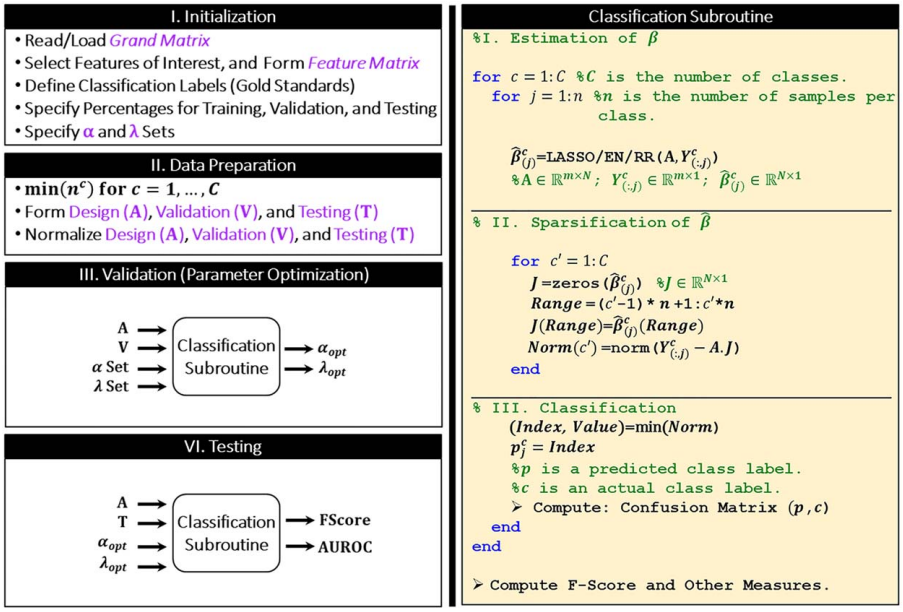

Fig. 6 A pseudo-code for the numerical implementation of the proposed SRC model, including the following steps: initialization, data preparation, validation (parameter optimization), and testing together with a classification subroutine. The subroutine is further composed of estimation and sparsification of the vector of membership coefficients (β) as well as of classification and computation of performance measures. LASSO, EN, and RR, respectively, stand for least absolute shrinkage and selection operator, elastic net, and ridge regression.

classification subroutine ultimately forms a confusion matrix and calculates several performance measures of the classifier, such as F-Score, the area under the receiver operating curve (AUROC), accuracy, recall, precision, specificity, informedness, markedness, and likelihood ratios.

2.2.5 Classification Subroutine. The right pane of Fig. 6 exhibits a pseudo-code for the numerical implementation of the classification subroutine. It is composed of three steps: (i) estimation of the vector of membership coefficients, $\hat{\boldsymbol{\beta}}$; (ii) sparsification of the $\hat{\boldsymbol{\beta}}$; and (iii) classification.

For each individual sample or observation per class, the input vector of classification features is constructed as follows: $\boldsymbol{Y}^c_{(:,j)} \in \mathbb{R}^{m\times 1}$ where $c = 1, 2, \ldots, C$ and $j = 1, 2, \ldots, n$; note that c is a class counter and j is a sample counter. Next, the vector of membership coefficients, $\hat{\boldsymbol{\beta}}^c_{(j)} \in \mathbb{R}^{N\times 1}$, is estimated using the LASSO, EN, or RR. The $\hat{\boldsymbol{\beta}}^c_{(j)}$ is subsequently sparsified and saved as a new vector ($\boldsymbol{J} \in \mathbb{R}^{N\times 1}$), which has nonzero elements only for the called class label, c. Then the approximation/fit error—called the *norm* mathematically, i.e., the error between the input vector of classification features, $\boldsymbol{Y}^c_{(:,j)}$, and the product of $\boldsymbol{A}\cdot\boldsymbol{J}$ ($\in \mathbb{R}^{m\times 1}$)—is calculated against all classes. The class, which leads to the lowest amount of error, is marked as a predicted class, p^c_j. Finally, based on the actual class (c) and predicted class (p), a confusion matrix is constructed, and then the main performance measures are calculated.

3 Experimental Results

In this section, we discuss experiments, designed and conducted to systematically assess the performance of the proposed SRC method for in situ and real-time estimation of line resistance, as delineated in Secs. 3.2 and 3.3, respectively.

AJP process parameters along with their complex interactions—which intrinsically and inevitably result in adverse phenomena, such as drift—influence the morphology, the resistance, and ultimately the functional integrity of printed electronics. This hierarchy is further illustrated using the following chain: process parameters (physical conditions) → line morphology (image captured) → line resistance (SRC estimated). Having set the physical conditions for material deposition, the morphology of an electronic trace, referred to as a "line" in this study, is captured using a series of images (as an image-based data stream) acquired in situ or in real-time. As discussed, these images reflect the most recent morphology of the line after deposition. Once processed, the image-based data stream (containing a wide spectrum of morphology traits) allows intelligent models (such as the SRC) to learn the dynamics of AJP and correlate the physical conditions (process parameters) as well as the morphological characteristics of the printed line with its functional properties (e.g., resistance). Incorporation of the physical knowledge behind the AJP process in the SRC model helps identify significant classification features; this would aid in (i) efficiently training the model, (ii) reducing computation time, and (iii) increasing classification accuracy.

There are two pathways to validate the results of resistance estimation using the SRC model: (i) directly via contrasting against offline probe measurements (Kelvin sensing) after sintering; (ii) via simulation of line morphology (instead of image acquisition) as a function of AJP process parameters using physical models (such as computational fluid dynamics (CFD)), and subsequently estimation of line resistance based on the simulation results using an intelligent model (such as the SRC).

According to Ohm's law, expressed by Eq. (7), the resistance (R, [Ω]) of an electronic is directly proportional to the length (L, [m]) and inversely proportional to the cross-sectional area (A, [m^2]), where the constant of proportionality is termed resistivity (ρ, [Ω.m]). The results of the SRC estimation of resistance can be linked to the physics of AJP and explained with a focus on the parameters that significantly influence line morphology, particularly line width, cross-sectional area, and perhaps line thickness

$$R = \rho\frac{L}{A} \tag{7}$$

3.1 Materials. A dry and pure (4.8 Grade) stream of N_2, flowing at ambient temperature (21 °C), is the primary medium of transport for both sheath and atomization gas flows.

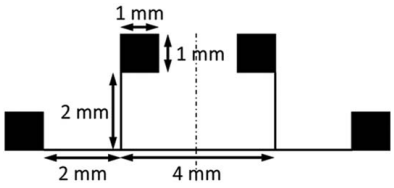

Fig. 7 The dimensions of the AJ-printed four-point probe electronic structures, composed of silver nanoparticles and deposited on a flexible polyimide substrate

For the in situ monitoring experiment (delineated in Sec. 3.2), a two-component silver nanoparticle ink, composed of MicroPEPG007MOP and MicroPEPG007EG (Paru Co., Seoul, Korea), was used to print four-point probe electronic structures (as schematically demonstrated in Fig. 7). The two components were mixed with a ratio of 5:1 by weight, accordingly. Both of the ink components have a particle size of 80 ± 10 nm.

- The first component is composed of silver nanoparticles (~66 wt%) and 1-methoxy-2-propanol (MOP) as solvent; it has a bulk density and viscosity of 1.5–2.5 g/ml and 50 cP, respectively.
- The second component is composed of silver nanoparticles (~33 wt%) and ethylene glycol (EG) as solvent; it has a bulk density and viscosity of 1.2–3.3 g/ml and 39 cP, respectively.

For the real-time monitoring experiment (delineated in Sec. 3.3), a single-component ink, i.e., PG007-AP (Paru Co., Seoul, Korea), was used. Composed of silver nanoparticles as well as 1-methoxy-2-propanol (MOP) as solvent, this ink has an average size, particle loading, and viscosity of 100 nm, ~60 wt%, and 100 cP, respectively.

The bubbler was filled with MOP to compensate for solvent evaporation during atomization, and thus to stabilize the ink viscosity. Prior to use, the ink was ultrasonically sonicated for approximately two minutes to obtain uniform dispersion of particles.

A sheet of polyimide (UPILEX 125S, Ube Plastics, Tokyo, Japan) was used as a flexible substrate, recommended for the manufacturing of flexible and hybrid electronics.

3.2 n Situ Monitoring of Line Resistance

3.2.1 Design and Analysis of Experiments. As detailed in Table 3, three single-factor factorial experiments were conducted under identical experimental conditions to observe the effects of: (i) ShGFR, (ii) EGFR, and (iii) PS on the morphological characteristics and the resistance of deposited four-point probe structures. A review of literature [13,20] reveals that ShGFR, PS, and carrier gas flowrate (CGFR) are controllable process parameters that influence line morphology significantly. The ShGFR aerodynamically collimates the stream of aerosols in AJP and as a result, affects line width as well as line thickness. PS controls the linear mass density of the deposited material (defined as mass per unit length [g/mm]) [13]. In addition, the CGFR (mathematically expressed as CGFR = AGFR − EGFR) controls the rate of aerosol transport and deposition; note that AGFR stands for atomization gas flow rate. When the pneumatic atomizer is utilized (like this study), the CGFR can be set via a combination of the following mechanisms: (i) using the AGFR and (ii) using the EGFR. Note that the AGFR controls the rate of pneumatic aerosol generating. The experiments presented in this study were designed and conducted under fixed atomization conditions. Consequently, the AGFR remained unchanged, and the EGFR was the controlling mechanism of the CGFR. The ShGFR, EGFR, and PS were varied randomly in the range of 40–100 sccm, 400–480 sccm, and 1–4 mm/s, respectively; the AGFR was fixed at 500 sccm. An equilibration time of five minutes was held between each set point change of ShGFR or EGFR to ensure steady-state transport and deposition of aerosols.

Utilizing the pneumatic atomizer and a nozzle, which has an internal exit diameter of 300 μm, the silver nanoparticle four-point probe structures (as schematically depicted in Fig. 7) were printed—repeated three times for each treatment combination of the experimental design—in a single pass on an unheated polyimide substrate. The choice of nozzle size was on the basis of previous studies [13,14,20] where pressure buildup and flow stagnation were identified as critical phenomena adversely influencing the stability of aerosol deposition in AJP. The working distance or print standoff (i.e., the distance between the nozzle and the substrate) was kept at 3 mm in all the experiments. The printed structures were oven-sintered (Binder, Inc., Bohemia, NY) for 1 h at 200 °C. The line resistance was measured using the four-point probe method via a source meter (Keithley-2614B, Tektronix, Inc., Beaverton, OR).

3.2.2 Experimental Observations. The high-resolution imaging system (introduced in Sec. 1.3.1) allows for in situ image acquisition from the deposited electronic structures. Once a line or a set of lines has been printed, the platen is rapidly translated under the CCD camera, and then images are captured from some or all parts of the printed structures as exemplified in Fig. 8. Subsequently, the acquired images are processed using processing algorithms, developed in-house in the environment of MATLAB and PYTHON; they are detailed in one of the authors' prior publications [13]. As categorized in Table 2, five characteristics of line morphology—including: line width, line density, edge quality/smoothness, overspray, and line discontinuity—in addition to 11 traits of image texture—including mean, standard deviation, smoothness, skewness, uniformity, entropy, contrast, correlation, energy, homogeneity, and max probability [48]—are extracted from the images. Besides, having transferred the images to undirected and unweighted network graphs, ten spectral graph-theoretic Laplacian

Table 3 AJP process parameters, materials, and experimental methods used to systematically investigate the influence of each factor on the morphology and the resistance of printed electronic structures

Parameter	Part I (ShGFR study)	Part II (EGFR study)	Part III (PS study)
ShGFR (sccm)	40, 60, 80, 100	60	60
EGFR (sccm)	450	400, 430, 450, 480	450
PS (mm/s)	4	4	1, 2, 3, 4
AGFR (sccm)	500	500	500
Atomizer type	Pneumatic	Pneumatic	Pneumatic
Nozzle size (μm)	300	300	300
Working distance (mm)	3	3	3
Ink	Silver NP	Silver NP	Silver NP
Substrate	Polyimide	Polyimide	Polyimide
Sintering type	Oven (1 h at 200 °C)	Oven (1 h at 200 °C)	Oven (1 h at 200 °C)
Resistance measurement	4-point probe	4-point probe	4-point probe

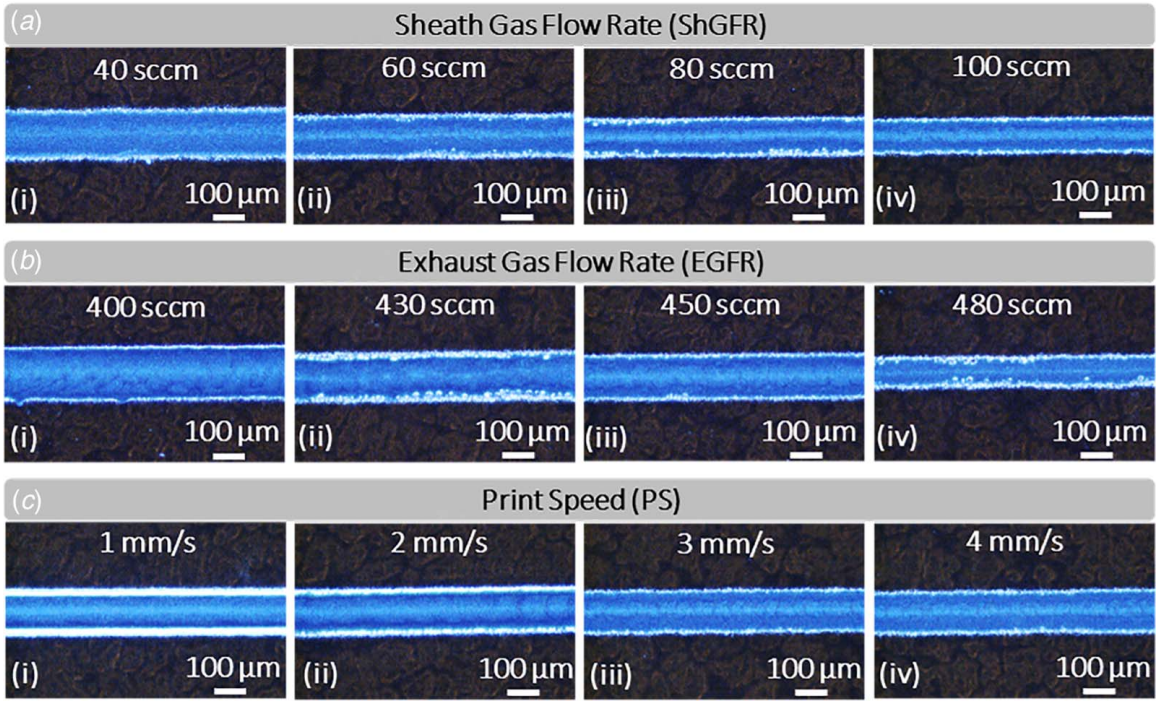

Fig. 8 A series of images captured in situ using the high-resolution CCD camera, demonstrating the effects of: (*a*) the ShGFR varying at four levels of 40, 60, 80, and 100 sccm, (*b*) the EGFR varying at four levels of 400, 430, 450, and 480 sccm, and (c) the PS varying at four levels of 1, 2, 3, and 4 mm/s, on the morphology of the deposited electronic traces. Note that sccm stands for standard cubic centimeter per minute.

eigenvalues [16], i.e., λ_2:λ_6—$\lambda_{end\text{-}4}$:λ_{end}, are extracted. We note that all of the aforementioned traits relate to the 2D morphology characteristics of the printed structures.

As visually observed from Fig. 8, the line width decreases significantly as the ShGFR and the EGFR increase. Note that the rate of decrease in the line width versus PS is relatively less prominent. No significant amount of overspray is observed under the set printing conditions (discussed in Table 3). The changes in the line width can be attributed to the following physical phenomena correspondingly, governing aerosol transport and deposition in AJP:

(i) The ShGFR directly influences collimation forces, which act externally on the aerosol stream.
(ii) The virtual impactor aerodynamically removes the bulk of the atomization gas and to a less significant extent, separates the droplets having relatively low linear momentum from the flow stream; as a result, a uniform dense stream of aerosols is delivered to the deposition head. The stronger the EGFR, the less the rate of aerosol transport (delivery) to the deposition head.
(iii) The PS inversely affects the linear mass density (mass per unit length) of the deposited structures.

The line width—unlike the line thickness and the CSA—is affected with the variation of the ShGFR, the EGFR, and the PS in a similar fashion. This stems from the fact that the ShGFR (unlike the EGFR and the PS) does not change the rate of material deposition per unit length but just the magnitude of the deposition collimation and thus density. As a result, denser and thicker lines are deposited as the ShGFR increases; this implies that less resistive lines are obtained. The trends reflected by the changes of the line width versus the ShGFR and PS are consistent with our previous observations [13,14], indicating the repeatability of the results.

It is expected that under the optimal experimental conditions (discussed in Sec. 3.2.1), the edge quality does not change significantly with the ShGFR and the EGFR but with the PS [13]. However, Figs. 8(*b-ii*) and 8(*b-iv*) indicate formation of rough edges after the aerosol deposition. An assignable cause was detected, revealing that such an anomaly in the edge smoothness stemmed from the presence of impurities on the surface.

Demonstrated in Fig. 8(*c-i*), the lines printed at the speed of 1 mm/s are of the highest quality characterized by smooth and uniform edges. The noticeable drop in the edge quality at the other PS's is due to the fact that the deposited aerosols do not completely reach receding, relaxation, and wetting equilibrium [21].

In addition to the aforementioned traits and experimental trends, two 3D morphology characteristics, i.e., the line thickness and the CSA, were quantified in situ, having recovered the 3D profile of the printed lines using the SfS image analysis [17], as exemplified in Fig. 9.

We note that the formation of highly reflective (bright) edges at the print speeds of 1 mm/s and 2 mm/s (see Figs. 8(*c-i*) and 8(*c-ii*)) results in the appearance of narrow valleys in their corresponding recovered surfaces (see Figs. 9(*c-i*) and 9(*c-ii*), respectively). In general, the adverse influence of the bright edges can be removed by, for example, high dynamic range imaging or diffuse illumination. We removed the background of the images to obtain a uniform ground reference for the quantification of the line thickness and the CSA.

The CSA was quantified by numerical integration of each 2D cross section, averaged over the entire line length. The authors' previous work regarding SfS [15] showed that Shah method [70] would perform well particularly when the direction of light source is comparable with that of camera (like our imaging system). Consequently, the Shah method was used in this study as the method of choice for the in situ reconstruction of the 3D cross-sectional profiles. Although not used in this study, several other traits—such as surface roughness parameters (*Ra*, *Rq*, and *Rt*)—were additionally quantified. While aiding in obtaining more accurate classification results, they would add more complexity to the model and thus, would increase computation time.

To corroborate the veracity of the in situ characterization of line morphology, the in situ (image-based) measurements of the width and the thickness of the AJ-printed lines were contrasted against offline measurements carried out using a white light interferometer (WLI). Implied from Fig. 10, both the in situ and the offline

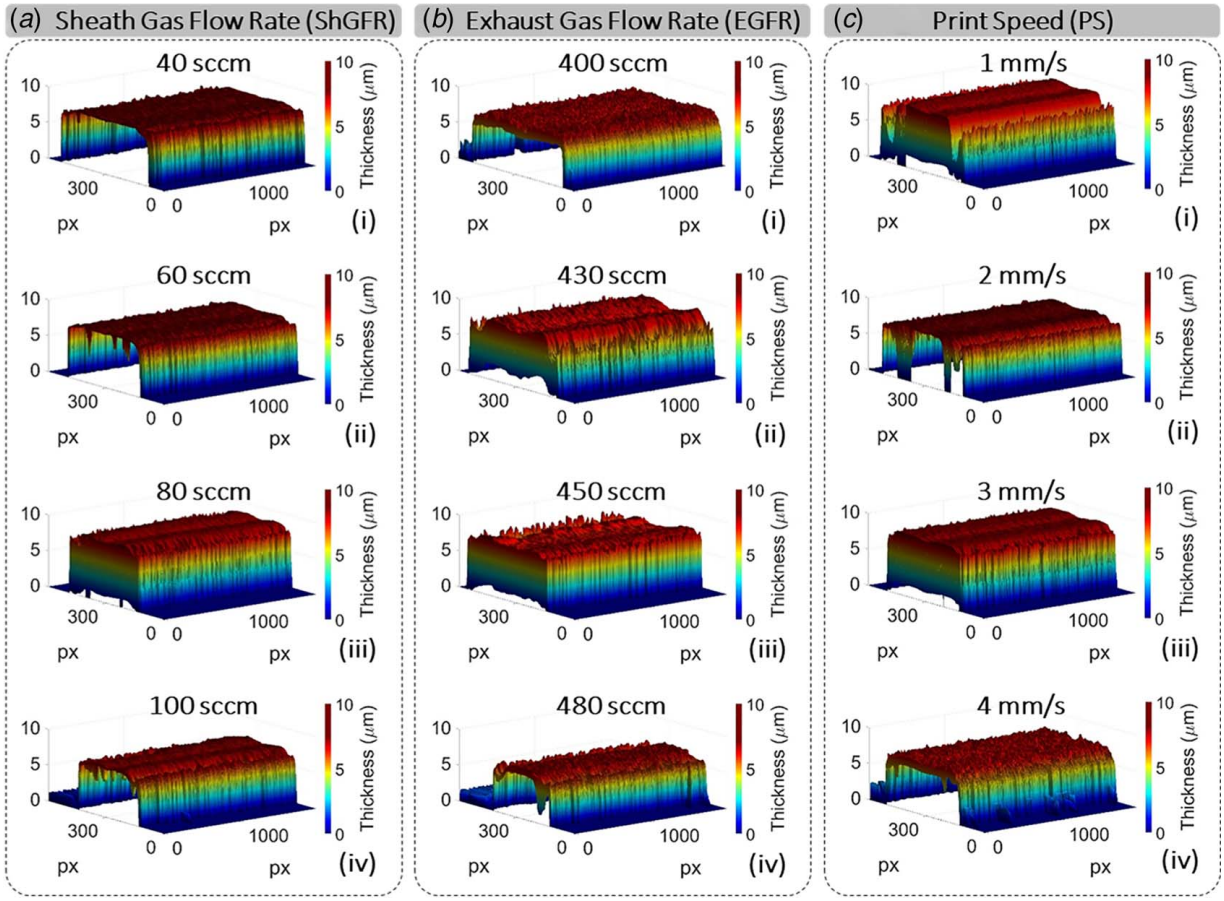

Fig. 9 Reconstruction of the 3D profile of the deposited electronic traces, using shape-from-shading analysis [17], allowing for quantification of the 3D morphology characteristics, e.g., the thickness and the cross-sectional area, as a function of: (*a*) the ShGFR varying at four levels of 40, 60, 80, and 100 sccm, (*b*) the EGFR varying at four levels of 400, 430, 450, and 480 sccm, and (*c*) the PS varying at four levels of 1, 2, 3, and 4 mm/s

measurements demonstrate similar trends, characterized with a correlation coefficient (ρ) of > 0.95. Note that the in situ thickness measurements were based on the SfS-reconstructed cross sections (illustrated in Fig. 9).

3.2.3 Classification of Line Resistance (L_R). The design matrix ($\mathbf{A} \in \mathbb{R}^{34\times720}$) is composed of 34 rows, i.e., $m = 34$ (representing the classification features, including the 31 line morphology traits, listed in Table 2, in addition to the three AJP process parameters), by 720 columns, i.e., $N = 720$ (representing observations or samples). The matrix is constructed as follows: there are four levels for each of the three factors (ShGFR, CGFR, and PS), designed to be repeated three times. From each of the 36 resulting experimental runs, an image was acquired. Each image was, subsequently, divided to 20 segments to populate enough samples for the training, validation, and testing datasets. Consequently, 720 samples were generated in total. The full field of view of the imaging system allows for capturing approximately 880 μm of the printed lines. The input vector of classification features ($\boldsymbol{Y} \in \mathbb{R}^{34\times1}$) is similarly composed of 34 rows, including all the 34 classification features.

Three class labels of line resistance, $C \in \{1, 2, 3\}$, were defined as follows; • Class 1: $L_R < 1.2\ \Omega$; • Class 2: $1.2\ \Omega \le L_R \le 1.6\ \Omega$; • Class 3: $L_R > 1.6\ \Omega$. 60% of the data (stored in the feature matrix) was randomly dedicated to training, 30% to validation, and 10% to testing. As discussed in Sec. 2.2, the grid spacing approach was employed to map a 2D space and thus to find the optimum values of λ and α, using the validation dataset, as exemplified in Fig. 11.

The results of the in situ SRC estimation of the line resistance are illustrated in Table 4 for a simulation run. The performance of the SRC model was evaluated based on F-Score, defined as the harmonic mean of precision and recall (sensitivity), as mathematically expressed by Eq. (8) [71,72]

$$F_{\text{Score}} = 2 \times \frac{(\bar{P} \cdot \bar{R})}{(\bar{P} + \bar{R})} \tag{8}$$

In Eq. (8), $\bar{P}$ and $\bar{R}$ stand for average precision and average recall, respectively; this is to generalize Eq. (8) for multiclass classification. Once a confusion matrix (**CM**) has been obtained (as exemplified in Table 4), the average values of the recall ($\bar{R}$) and the precision ($\bar{P}$) are calculated as detailed in Eqs. (9)–(12). Note that m and n represent the number of rows and columns of the confusion

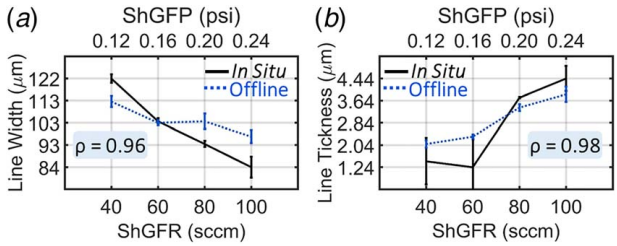

Fig. 10 Validation of the in situ characterization of line morphology, demonstrated as a comparison between in situ (image-based) and offline (WLI-based) measurements of: (*a*) the width as a 2D morphology trait, and (*b*) the thickness as a 3D morphology trait of the AJ-printed lines, exhibiting similar trends (having a Pearson's correlation coefficient, ρ, of 0.96 and 0.98, respectively). WLI stands for white light interferometry.

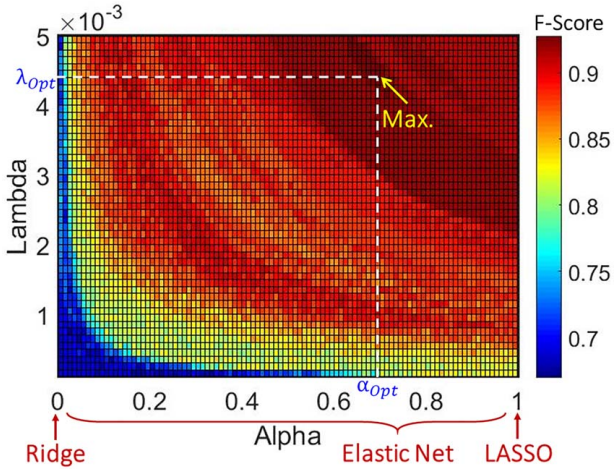

Fig. 11 A 2D parameter optimization space, obtained using a grid spacing (heuristic) approach, which indicates the optimal values of the regularization parameter (λ) and the weighting parameter (α). These two values are subsequently used to classify a testing dataset

matrix (**CM**), respectively. Furthermore, $\boldsymbol{R} \in \mathbb{R}^{m\times 1}$ and $\boldsymbol{P} \in \mathbb{R}^{1\times n}$ are the recall vector and the precision vector, correspondingly. $\boldsymbol{R}_0$ and $\boldsymbol{P}_0$ represent the ℓ_0-norm (i.e., the number of elements) of the recall and precision vectors, respectively

$$\boldsymbol{R}_{(i)} = \frac{\mathbf{CM}_{(i,i)}}{\sum_{j=1}^{n} \mathbf{CM}_{(i,j)}} \quad \text{for } i = 1, 2, \ldots, m \tag{9}$$

$$\bar{R} = \frac{\sum_{i=1}^{m} \boldsymbol{R}_{(i)}}{\|\boldsymbol{R}\|_0} \tag{10}$$

$$\boldsymbol{P}_{(j)} = \frac{\mathbf{CM}_{(j,j)}}{\sum_{i=1}^{m} \mathbf{CM}_{(i,j)}} \quad \text{for } j = 1, 2, \ldots, n \tag{11}$$

Table 4 The results of a single classification simulation, performed to estimate the resistance of printed electronic structures, based on in situ image data

Sparse estimation classification Optimal method: LASSO		Estimated condition		
		Class 1	Class 2	Class 3
True condition	Class 1 (24)	100% (24)	0% (0)	0% (0)
	Class 2 (24)	0% (0)	96% (23)	4% (1)
	Class 3 (24)	0% (0)	8% (2)	92% (22)
Classification measures	Recall	100%	96%	92%
	Precision	100%	92%	96%
	False alarm	0%	4%	2%
	Specificity	100%	96%	98%
Optimization	λ (Opt)		0.0031	
	α (Opt)		1.00	
Performance evaluation	F-Score		95.9%	

Note: In this simulation, the LASSO was automatically chosen by the parameter optimization algorithm, based on the value of $\alpha = 1$. The elastic net and ridge regression methods would have been alternatively chosen, had the weighting parameter been $0 < \alpha < 1$ and $\alpha \approx 0$, respectively. The numbers in the parentheses demonstrate the number of classified samples per class label.

$$\bar{P} = \frac{\sum_{j=1}^{n} \boldsymbol{P}_{(j)}}{\|\boldsymbol{P}\|_0} \tag{12}$$

The SRC model was run 100 times to avoid the intrinsic bias of the model, resulting from the random partitioning of the training, validation, and testing datasets. As a result, an average F-Score of 0.95 ± 0.005 was obtained with consideration of a significance level of 0.05. This implies that the line resistance can be estimated in situ with an accuracy of approximately 95%. The performance of the model can be further improved by an optimal selection of the classification features. While the selection of a larger number of the features may result in improved performance, it adversely increases computation time (particularly during the process of training and validation).

3.2.4 Overall Assessment of the Performance. As illustrated in Fig. 12(*a*), the performance of the SRC model was contrasted systematically against that of seven well-known classifiers—including ANN [73], DT [74], DA [75], NB [76,77], kNN [78], SVM [79–82], and ensemble of learners (Ens) [83,84]—versus three to six class labels of the line resistance.

Figure 12(*a*) demonstrates that as the number of class labels increases, the performance of all the models decreases (in a dissimilar fashion). Comparing the first and last class labels, a 27% reduction in performance was observed for the ANN; similarly, both the NB and the SVM approximately exhibited a 25% reduction in their performance. The reduction in the performance of the SRC model was comparable with the DTs and the KNNs, being about 11%. The Ens had the smallest performance reduction, i.e., approximately 8%. It is worth mentioning that the DA displayed a relatively moderate performance reduction of about 18%.

It was observed that the ANN, unlike the other classifiers, was not capable of classifying the line resistance when the number of class

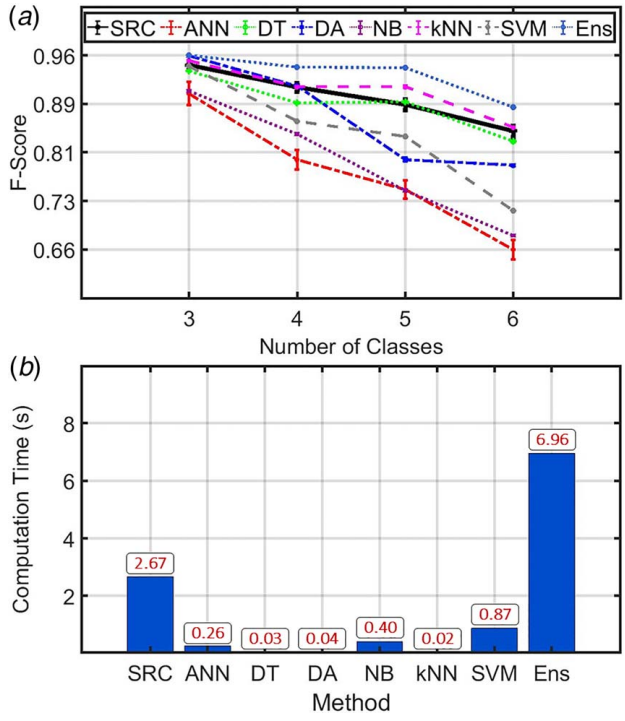

Fig. 12 A comparison between: (*a*) the performance and (*b*) the computation time of the SRC model and those of several other well-known classifiers including ANN, DT, DA, NB, kNN, SVM, and ensemble of learners (Ens). The error bars represent 95% confidence intervals around the F-Score means.

labels was greater than six (the trend is not shown); this is because both the precision and the recall were zero, resulting in an undefined value (NaN) in the calculation of the F-Score, expressed by Eq. (8). The accuracy of the SRC model is comparable to that of the kNN and the DT, following the accuracy of the Ens classifier. Note that the Ens consists of a weighted combination of multiple classifiers; such a combination leads to an increase in the predictive performance.

In addition to the comparative performance assessment, all the classifiers were relatively compared with respect to their computation times (including the three steps of training, validation, and testing), as demonstrated in Fig. 12(*b*). The kNN, the DT, and the DA had the smallest computation times (being in the order of a few hundredths of a second per simulation run); note that the kNN's performance was comparable with the SRC's (implied from Fig. 12(*a*)). The SVM, the NB, and the ANN exhibited intermediate computation times, i.e., approximately a few tenths of a second, which were one order of magnitude smaller than those of the SRC and the Ens. These computation times were obtained from the classification of the same set of data into five a priori class labels (as presented in Fig. 12(*a*)). This comparison is forwarded here just to provide rough estimates about the computation time of each model. Since their background algorithms are not optimized at the same level, no strict conclusions can be further deduced from the observed trends. Overall, based on the analysis of the performance and the computation time of the aforementioned models, it is concluded that the SRC model can be used as a robust high-performance classifier for the in situ estimation of line resistance in AJP process.

In real-time applications, only the computation time of "testing" will be critical—reflecting the true computation time of a classifier—since both training and validation are implemented prior to the start of monitoring a process. Apropos of AJP process monitoring, there are inevitable delays, which make the whole monitoring process "near real-time," stemming from image acquisition, storage, processing, offset in observation [85], and stage translation in addition to classification.

3.3 Real-time Monitoring of Line Resistance

3.3.1 Design and Analysis of Experiments. As discussed in Sec. 1.3, the new experimental setup configuration—utilizing the standard process monitor camera instead of the integrated CCD camera—allows for image acquisition, processing, and ultimately estimation of line functional properties in near real-time. Note that the term "near real-time" is used to emphasize that due to the inherent delays in the AJP process (as discussed in Sec. 3.2.4), the SRC model is capable of estimating line resistance and/or other functional properties near (not exactly at) the time of aerosol deposition.

In order to further assess the robustness of the model, a two-factor factorial experiment was designed where the print speed (PS) was changed randomly at three levels of 2, 4, and 6 mm/s, each at two ShGFR levels of 40 and 60 sccm. In addition, each treatment combination of the experimental design was repeated five times (resulting in 30 runs, in total). The two pneumatic atomization parameters, i.e., the AGFR and the EGFR, were set at 640 and 610 sccm, respectively. A 200 μm nozzle tip was used to print enhanced four-point probe structures, as schematically illustrated in Fig. 13(*c*), where all of the four pads were post-deposited at the same horizontal level with a speed of 4 mm/s to reduce the printing time and thus to minimize the adverse, uncontrollable effects of the AJP process drift.

Under constant illumination conditions, images were acquired from the central line of the printed structures (15 mm long) while the deposition of material, with a frame rate of 50 fps and exposure time of approximately 1 ms, as exemplified in Figs. 13(*a*) and 13(*b*). The field of view of the camera was narrowed to a window of 100 × 300 px (which approximately corresponds to 100 × 300 μm using a calibration factor of 1.01 μm/px) to: (i) restrict the image acquisition window only to the depth of field and (ii) obtain an optimal image size for characterization of the morphology of the printed structures. This means that only 100 μm of the line length could be observed per frame. However, based on the set frame rate of 50 fps as well as the PS of 2, 4, and 6 mm/s, correspondingly 40, 80, and 120 μm of the line length are traveled between two consecutive images. In other words, at the PS of 2 and 4 mm/s, oversampling is occurring, while at the PS of 6 mm/s, image acquisition is influenced by unavoidable undersampling (i.e., loss of information in areas not imaged). Consequently, to prevent oversampling between images, the oversampled areas were cropped before the morphology characterization, adjusted according to their corresponding PSs. The same image processing logic and routines, discussed in Sec. 3.2.2, were applied to the cropped images to extract the morphology traits.

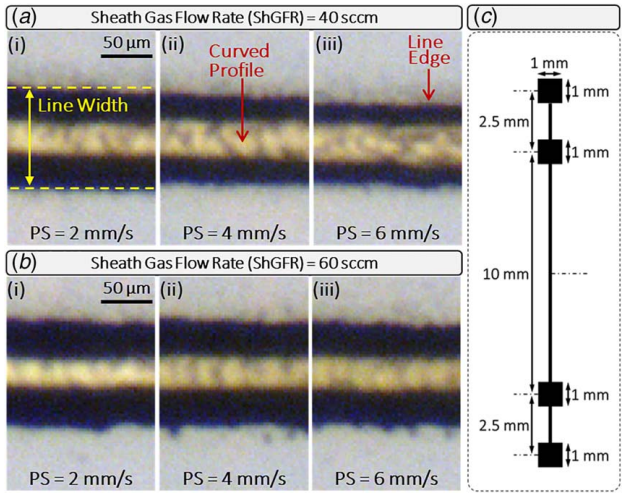

Fig. 13 (*a*, *b*) True-color images captured in real-time using the AJP process monitor camera with a frame rate of 50 fps and an exposure time of 1 ms, windowed to a field of view of 100 × 300 μm and (c) the dimensions of the modified four-point probe electronic structures

Integrated with the SRC model, the image processing algorithms allow for morphology characterization of electronics with noncomplex geometrical features. The SRC model, itself, is computationally fast and can handle image data streams with low signal-to-noise ratio. The solution to the challenge of real-time monitoring of the functional properties of electronics with complex morphological traits is twofold: (i) more sophisticated image processing algorithms need to be forwarded; (ii) use of advanced image-based sensors, e.g., infrared and thermal cameras (perhaps together with temporal sensors), would allow for more accurate detection of the boundaries of a component (which might overlap another previously deposited component), as well as for monitoring the dynamics of material deposition in AJP, for example, by image-based tracking of the amount of solvent evaporation from deposited material. Furthermore, complex electronics usually have simple interconnects (line traces) that represent the overall morphology and thus may be potentially used for monitoring the functional properties. Note that the use of interconnect features or test coupons may adversely influence the frequency of process monitoring (because of inherent delays, stemming from stage translation for example); as a result, there is a trade-off between feature simplicity and monitoring frequency.

3.3.2 Experimental Observations. Having deposited the samples, they were baked in a convection oven at 200 °C for 1 h (plus 20 min dedicated to temperature ramp-up). Subsequently, the resistance of the printed structures was measured using the four-

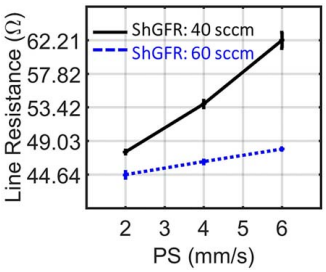

Figure 14 Line resistance versus print speed (PS), plotted at two levels of the ShGFR (40 and 60 sccm). The error bars are ($\pm 1\sigma$) long where σ is the standard deviation of the measurements.

point probe method, as plotted versus PS at the two levels of the ShGFR in Fig. 14.

Equation (7) can be rewritten with consideration of the volume flowrate of material deposition ($\dot{V}$) [m^3/s]—expressed as $\dot{V} = PS \cdot A$, where PS stands for print speed [m/s], and A represents the cross-sectional area of a deposited line [m^2]—as follows:

$$R = \frac{\rho \cdot L \cdot PS}{\dot{V}} \tag{13}$$

If the ShGFR is constant, the volume flowrate of material deposition ($\dot{V}$) will be constant as well—because both the AGFR and the EGFR are constant in this experiment, as mentioned in Sec. 3.3.1—if we assume all other factors and experimental conditions remain constant. Please also note that the length of the printed lines (L) is fixed at 10 mm (see Fig. 13). Consequently, if $\dot{V}$ is constant, Eq. (13) can be re-written, as follows, where $\left(\frac{\rho \cdot L}{\dot{V}}\right)$ represents the slope

$$R = \left(\frac{\rho \cdot L}{\dot{V}}\right) PS \tag{14}$$

Such a linear relationship between R and PS is observed in Fig. 14 at the two ShGFR levels. If the ShGFR changes, $\dot{V}$ changes to some extent, and as a result, the slope changes (compare the dashed line with the solid line). The demonstrated trends were juxtaposed with the results of a study by Mahajan et al. [20], which corroborates the veracity of the observed trends.

Figure 14 indicates that the PS has much more significant influence on the line resistance at the ShGFR of 40 sccm compared with 60 sccm (i.e., almost a 30% increase in the line resistance from 2 to 6 mm/s at 40 sccm versus only a 7% increase at 60 sccm). This is an implication of the fact that there is a strong interaction between the PS and the ShGFR. In other words, there exists a nonlinear relationship between the line resistance (as the response variable) and the two factors. This hypothesis was statistically tested and affirmed using analysis of variance. The analysis demonstrated that the ShGFR and the PS as well as their interactions were statistically significant at 1% level of significance. Figure 14 aids in locating the optimal values of the line resistance. For example, material deposition at low levels of the PS and high levels of the ShGFR results in the most conductive structures (characterized by narrow and thick lines).

The effect of PS is to spread the same amount of material (under fixed material deposition rate) over a longer distance when it increases. While influencing line morphology and thus line resistance, it does not directly affect the material deposition rate in the same manner as the sheath and atomization gas flowrates; consequently it should be considered as a second-order parameter to resistance.

Due to the spreading effect of PS, the deposition and coalescence of aerosols are affected significantly (at high PSs); this leads to formation of discontinuous lines, characterized with poor edge quality as well as low line density. To investigate this phenomenon, a

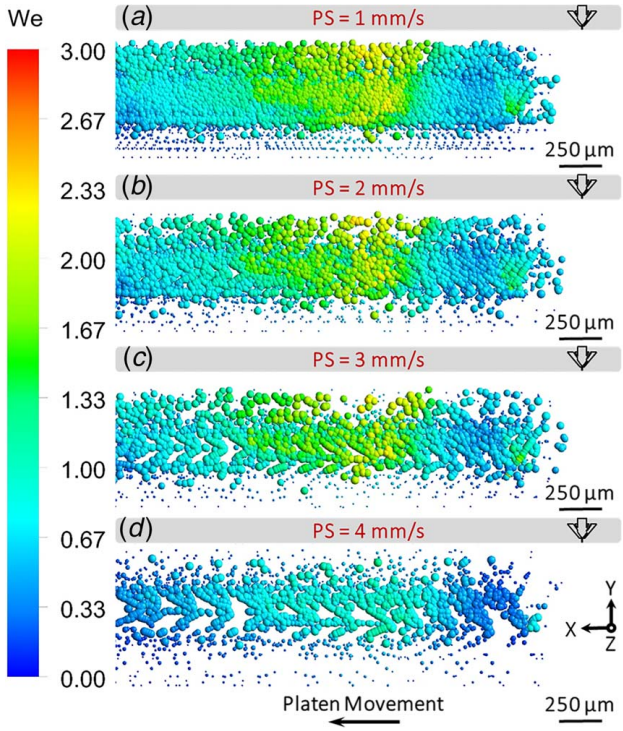

Fig. 15 A CFD simulation of the influence of print speed (PS), varying at four levels of: (*a*) 1 mm/s, (*b*) 2 mm/s, (*c*) 3 mm/s, and (*d*) 4 mm/s, on AJ-printed trace morphology, demonstrating the impingement and post-deposition coalescence of aerosols on a moving free surface. An increase in the Weber number (We) is indicative of the fact that that the aerosols contribute to the line formation more significantly (by sticking to the wall film).

compressible, turbulent multiphase flow CFD model was forwarded. We delineated the governing mathematical equations and the boundary conditions behind the CFD model in details in Refs. [13,86]. As demonstrated in Fig. 15, the line morphology is adversely affected when the PS increases from 1 to 4 mm/s. This stems from the spreading effect of the PS, which deprives the impinging aerosols of initial wall film formation, subsequent coalescence, and ultimately formation of a continuous line trace. This phenomenon is evident when Figs. 15(*a*)–15(*d*) are compared. In addition, tracking the Weber number (We) of the aerosols—defined as the ratio of the inertia of a fluid to the surface tension—revealed that the aerosols contribute to the formation of the thin wall film (and thus the line trace) less significantly when the PS increases.

3.3.3 Classification of Line Resistance. Based on the measurements of the resistance (falling in a wide range between approximately 44–62 Ω), five distinct class labels were defined, as follows: • Class 1: 44.0 Ω ≤ L_R < 45.5 Ω; • Class 2: 45.5 Ω ≤ L_R < 47.0 Ω; • **Class 3:** 47.0 Ω ≤ L_R < 48.5 Ω; • Class 4: 50.0 Ω ≤ L_R < 60.0 Ω; and • Class 5: L_R ≥ 60.0 Ω. Note that these labels were defined to pose a real case study and subsequently, to assess the performance of the SRC model. In this experiment, we followed the same procedure for the setup and implementation of the SRC model as the one used in the in situ monitoring experiment (detailed in Sec. 3.2.3). As mentioned in Sec. 3.3.1, there are six treatment (factor) combinations, each repeated five times, resulting in 30 experimental runs. From each of the 30 runs of the randomized experimental design, 30 images were selected and subsequently processed, leading to 900 samples (image-based data) available in total for the analysis. As already discussed in Sec. 2.2, the SRC model requires allocation of an equal number of samples per class; consequently, this limitation reduced the total number of samples to 750. As a result, 450 (60%), 225 (30%), and 75 (10%)

Table 5 The results of a single classification simulation, performed to estimate the resistance of printed electronic structures, based on real-time image data

Sparse estimation classification Optimal method: LASSO		Estimated condition				
		Class 1	Class 2	Class 3	Class 4	Class 5
True condition	Class 1 (15)	87% (13)	7% (1)	7% (1)	0% (0)	0% (0)
	Class 2 (15)	0% (0)	100% (15)	0% (0)	0% (0)	0% (0)
	Class 3 (15)	0% (0)	0% (0)	93% (14)	7% (1)	0% (0)
	Class 4 (15)	0% (0)	0% (0)	0% (0)	93% (14)	7% (1)
	Class 5 (15)	0% (0)	0% (0)	0% (0)	0% (0)	100% (15)
Classification measures	Recall	86.67%	100%	93.33%	93.33%	100%
	Precision	100%	93.75%	93.33%	93.33%	93.75%
	False alarm	0%	1.67%	1.64%	1.64%	1.67%
	Specificity	100%	98.33%	98.36%	98.36%	98.33%
Optimization	λ (Opt)			0.005		
	α (Opt)			1.00		
Performance evaluation	F-Score			94.75%		

Note: In this simulation, the LASSO was automatically chosen by the parameter optimization algorithm, based on the value of $\alpha = 1$. The numbers in the parentheses demonstrate the number of classified samples per class label.

samples were dedicated to the training, validation, and testing of the model, respectively. Table 5 exemplify a confusion matrix, demonstrating various measures of the performance of the model, including recall (sensitivity), precision, false alarm rate, specificity (selectivity), as well as F-Score for a single simulation. To avoid the intrinsic bias of the model, resulting from the random partitioning of the data, the model was run 25 times (with random data allocation per simulation), resulting in an F-Score of 0.92 ± 0.013.

Furthermore, a tenfold cross-validation procedure was used to check the robustness of the model; an F-Score of 0.96 ± 0.017 was obtained. In addition to the F-Score, the AUROC—extended to multilabel classification by calculating for all possible combinations of class labels—was used as a second measure of classification accuracy. Similarly, having run the SRC model 25 times, an average AUROC of 0.96 ± 0.006 was obtained. Overall, both the F-Score and the AUROC imply that the presented SRC model is capable of estimating line resistance (and potentially, other functional properties) in near real-time with an accuracy of ≥ 0.90.

4 Conclusion and Future Work

In this study, an intelligent learning model was forwarded, based on the concept of sparse representation for classification (SRC), to estimate the functional properties (e.g., resistance) of printed electronics. An integrated high-resolution CCD camera and the AJP standard process monitor camera were used respectively for in situ and real-time image acquisition. A wide range of image processing algorithms, developed in-house, were also used to extract 2D and 3D line morphology traits; they together with AJP process parameters constituted the classification features. The presented SRC model is based on a new convex optimization formulation—consisting of not only the ℓ_2-norm of the fit error but also the ℓ_1-norm and ℓ_2-norm of the vector of membership coefficients—solved using a combination of the LASSO, elastic net, and ridge regression. The model was validated using in situ and real-time designed experiments, where four-point probe electronic structures were deposited as a functional of influential process parameters. A priori class labels were defined based on the resistance of the printed structures. The performance and computation time of the model was contrasted against that of seven well-known classifiers. Overall, the results of this study corroborated that the proposed SRC model could accommodate the multivariate and heterogonous nature of AJP sensor data and thus, be used for in situ as well as real-time estimation of the resistance (and potentially, other functional properties) of printed electronics with an accuracy of ≥ 0.90.

The following avenues for future work will be explained in the forthcoming publications:

(1) The computer algorithms and routines, forwarded in this work for both image processing and the SRC estimation of line resistance, will be optimized for implantation of closed-loop control of functional properties in AJP; the goal will be to achieve controlled, conformal deposition of electronics with uniform functional properties.
(2) Currently, there are approximately 60 2D and 3D morphology traits, extracted from an acquired image. The performance of the SRC model will be further optimized by an optimal selection of the classification features, for example, with the aid of dimensional reduction techniques (e.g., principle component analysis) to avoid unnecessary processing of large data sets.
(3) A CFD mode will be forwarded to explain the underlying physical phenomena behind the experimental observations discussed in this work. This allows for mapping of velocity and pressure fields as well as particle trajectories, and thus simulation of line morphology particularly in critical conditions (e.g., at high atomization gas flowrates) where conducting an experiment is time-consuming and expensive.
(4) Finally, this study will be augmented to include other consequential factors and process parameters (e.g., ink viscosity, surface energy, and nozzle size).

Acknowledgment

This material is based upon work supported, in part, by Air Force Research Laboratory under agreement number FA8650-15-2-5401. The U.S. Government is authorized to reproduce and distribute reprints for Governmental purposes notwithstanding any copyright notation thereon. The views and conclusions contained herein are those of the authors and should not be interpreted as necessarily representing the official policies or endorsements, either expressed or implied, of Air Force Research Laboratory or the U.S. Government.

The authors would also like to sincerely acknowledge the Small Scale Systems Integration and Packaging (S^3IP), the Center for Advanced Microelectronics Manufacturing (CAMM), the Center for Flexible Hybrid Medical Device Manufacturing (FlexMed), and the Analytical and Diagnostics Lab (ADL) at the State University of New York (SUNY) at Binghamton.

One of the authors (Prahalada Rao) thanks the National Science Foundation (NSF) for funding his research and educational thrusts through grants OIA-1929172, CMMI-1719388, CMMI-1920245,

CMMI-1739696, and CMMI-1752069 (CAREER). The idea of using in-process sensor-based monitoring and machine learning for real-time detection of flaws in additively manufactured parts during the printing processes was proposed and funded in CMMI-1752069 (CAREER, Program Officer: Dr. Khershed P. Cooper). Supplemental funding for the CAREER through the NSF INTERN (Program Office: Dr. Prakash Balan) program and CMMI Data Science Activities funding (Program Officer: Dr. Martha Dodson) is greatly appreciated.

References

[1] Parekh, D. P., Cormier, D., and Dickey, M. D., 2015, "Chapter 8: Multifunctional Printing: Incorporating Electronics Into 3D Parts Made by Additive Manufacturing," *Additive Manufacturing*, A. Bandyopadhyay, and S. Bose, eds., CRC Press, Boca Raton, FL, p. 215.
[2] Jones, C. S., Lu, X., Renn, M., Stroder, M., and Shih, W.-S., 2010, "Aerosol-Jet-Printed, High-Speed, Flexible Thin-Film Transistor Made Using Single-Walled Carbon Nanotube Solution," Microelectron. Eng., **87**(3), pp. 434–437.
[3] Kim, S. H., Hong, K., Lee, K. H., and Frisbie, C. D., 2013, "Performance and Stability of Aerosol-Jet-Printed Electrolyte-Gated Transistors Based on Poly (3-Hexylthiophene)," ACS Appl. Mater. Interfaces, **5**(14), pp. 6580–6585.
[4] Liu, R., Shen, F., Ding, H., Lin, J., Gu, W., Cui, Z., and Zhang, T., 2013, "All-Carbon-Based Field Effect Transistors Fabricated by Aerosol Jet Printing on Flexible Substrates," J. Micromech. Microeng., **23**(6), p. 065027.
[5] Goth, C., Putzo, S., and Franke, J., "Aerosol Jet Printing on Rapid Prototyping Materials for Fine Pitch Electronic Applications," Proceedings of IEEE Electronic Components and Technology Conference (ECTC), Lake Buena Vista, FL, May 31–June 3, pp. 1211–-1216.
[6] Liu, R., Ding, H., Lin, J., Shen, F., Cui, Z., and Zhang, T., 2012, "Fabrication of Platinum-Decorated Single-Walled Carbon Nanotube Based Hydrogen Sensors by Aerosol Jet Printing," Nanotechnology, **23**(50), p. 505301.
[7] Zhao, D., Liu, T., Zhang, M., Liang, R., and Wang, B., 2012, "Fabrication and Characterization of Aerosol-Jet Printed Strain Sensors for Multifunctional Composite Structures," Smart Mater. Struct., **21**(11), p. 115008.
[8] Tait, J. G., Witkowska, E., Hirade, M., Ke, T.-H., Malinowski, P. E., Steudel, S., Adachi, C., and Heremans, P., 2015, "Uniform Aerosol Jet Printed Polymer Lines With 30 μm Width for 140 ppi Resolution RGB Organic Light Emitting Diodes," Org. Electron., **22**(7), pp. 40–43.
[9] Eckstein, R., Hernandez-Sosa, G., Lemmer, U., and Mechau, N., 2014, "Aerosol Jet Printed Top Grids for Organic Optoelectronic Devices," Org. Electron., **15**(9), pp. 2135–2140.
[10] Hon, K., Li, L., and Hutchings, I., 2008, "Direct Writing Technology—Advances and Developments," CIRP Ann., **57**(2), pp. 601–620.
[11] King, B., and Renn, M., 2009, "Aerosol Jet Direct Write Printing for Mil-Aero Electronic Applications," Proceedings of Lockheed Martin Palo Alto Colloquia, Palo Alto, CA, Mar. 26, pp. 1–6.
[12] Gu, Y., Gutierrez, D., Das, S., and Hines, D., 2017, "Inkwells for On-Demand Deposition Rate Measurement in Aerosol-Jet Based 3D Printing," J. Micromech. Microeng., **27**(9), p. 097001.
[13] Salary, R., Lombardi, J. P., Tootooni, M. S., Donovan, R., Rao, P. K., Borgesen, P., and Poliks, M. D., 2017, "Computational Fluid Dynamics Modeling and Online Monitoring of Aerosol Jet Printing Process," ASME J. Manuf. Sci. Eng., **139**(2), p. 021015.
[14] Salary, R., Lombardi, J. P., Tootooni, M. S., Donovan, R., Rao, P. K., and Poliks, M. D., 2016, "In Situ Sensor-Based Monitoring and Computational Fluid Dynamics (CFD) Modeling of Aerosol Jet Printing (AJP) Process," ASME 2016 11th International Manufacturing Science and Engineering Conference (MSEC 2016), Virginia Tech, Blacksburg, VA, June 27—July 1, Proc. Paper No. 8535, p. V002T004A049.
[15] Salary, R., Lombardi, J., Rao, P., and Poliks, M. D., 2017, "Online Monitoring of Functional Electrical Properties in Aerosol Jet Printing Additive Manufacturing Process Using Shape-From-Shading Image Analysis," ASME J. Manuf. Sci. Eng., **139**(10), p. 101010.
[16] Rao, P. K., Beyca, O. F., Kong, Z., Bukkaptanam, S. T. S., Case, K. E., and Komanduri, R., 2015, "A Graph Theoretic Approach for Quantification of Surface Morphology and Its Application to Chemical Mechanical Planarization (CMP) Process," IIE Trans., **47**(10), pp. 1088–1111.
[17] Salary, R., Lombardi, J. P., Rao, P. K., and Poliks, M. D., 2017, "Additive Manufacturing (AM) of Flexible Electronic Devices: Online Monitoring of 3D Line Morphology in Aerosol Jet Printing Process Using Shape-From-Shading Image Analysis," ASME 2017 12th International Manufacturing Science and Engineering Conference (MSEC 2017), University of Southern California, Los Angeles, CA, June 4–8, Proc. Paper No. 2947, p. V002T001A046.
[18] Lombardi, J. P., Salary, R., Weerawarne, D. L., Rao, P. K., and Poliks, M. D., 2018, "In Situ Image-Based Monitoring and Closed-Loop Control of Aerosol Jet Printing," ASME 2018 13th International Manufacturing Science and Engineering Conference (MSEC 2018), Texas A&M University, College Station, TX, June 18–22, Proc. Paper No. 6487.
[19] Wadhwa, A., 2015, "Run-time Ink Stability in Pneumatic Aerosol Jet Printing Using a Split Stream Solvent Add Back System," M.S. thesis, Advisor: Denis Cormier, Department of Industrial and Systems Engineering, Rochester Institute of Technology.
[20] Mahajan, A., Frisbie, C. D., and Francis, L. F., 2013, "Optimization of Aerosol Jet Printing for High-Resolution, High-Aspect Ratio Silver Lines," ACS Appl. Mater. Interfaces, **5**(11), pp. 4856–4864.
[21] Feng, J. Q., 2016, "A Computational Study of High-Speed Microdroplet Impact Onto a Smooth Solid Surface," Cornell University Library, Physics-Fluid Dynamics, Xiv:1602.07672.
[22] Kothuru, A., Nooka, S. P., and Liu, R., 2018, "Audio-based Tool Condition Monitoring in Milling of the Workpiece Material with the Hardness Variation Using Support Vector Machines and Convolutional Neural Networks," ASME J. Manuf. Sci. Eng., **140**(11), p. 111006.
[23] Wu, D., Jennings, C., Terpenny, J., Kumara, S., and Gao, R. X., 2018, "Cloud-based Parallel Machine Learning for Tool Wear Prediction," ASME J. Manuf. Sci. Eng., **140**(4), p. 041005.
[24] Khanzadeh, M., Rao, P., Jafari-Marandi, R., Smith, B. K., Tschopp, M. A., and Bian, L., 2018, "Quantifying Geometric Accuracy with Unsupervised Machine Learning: Using Self-Organizing Map on Fused Filament Fabrication Additive Manufacturing Parts," ASME J. Manuf. Sci. Eng., **140**(3), p. 031011.
[25] Li, Z., Wu, D., and Yu, T., 2019, "Prediction of Material Removal Rate for Chemical Mechanical Planarization Using Decision Tree-Based Ensemble Learning," ASME J. Manuf. Sci. Eng., **141**(3), p. 031003.
[26] Du, J., Yue, X., Hunt, J. H., and Shi, J., 2019, "Optimal Placement of Actuators Via Sparse Learning for Composite Fuselage Shape Control," ASME J. Manuf. Sci. Eng., **141**(10), p. 101004.
[27] He, A., and Jin, X., 2019, "Failure Detection and Remaining Life Estimation for Ion Mill Etching Process Through Deep-Learning Based Multimodal Data Fusion," ASME J. Manuf. Sci. Eng., **141**(10), p. 101008.
[28] Imani, F., Chen, R., Diewald, E., Reutzel, E., and Yang, H., 2019, "Deep Learning of Variant Geometry in Layerwise Imaging Profiles for Additive Manufacturing Quality Control," ASME J. Manuf. Sci. Eng., **141**(11), p 111001.
[29] Han, C., Luo, M., Zhang, D., and Wu, B., 2018, "Iterative Learning Method for Drilling Depth Optimization in Peck Deep-Hole Drilling," ASME J. Manuf. Sci. Eng., **140**(12), p. 121009.
[30] Candès, E. J., and Wakin, M. B., 2008, "An Introduction to Compressive Sampling," IEEE Signal Process. Mag., **25**(2), pp. 21–30.
[31] Wright, J., Yang, A. Y., Ganesh, A., Sastry, S. S., and Ma, Y., 2009, "Robust Face Recognition via Sparse Representation," IEEE Trans. Pattern Anal. Mach. Intell., **31**(2), pp. 210–227.
[32] Barazandeh, B., Bastani, K., Rafieisakhaei, M., Kim, S., Kong, Z., and Nussbaum, M. A., 2017, "Robust Sparse Representation-Based Classification Using Online Sensor Data for Monitoring Manual Material Handling Tasks," IEEE Trans. Autom. Sci. Eng., **15**(4), pp. 1573–1584.
[33] Bastani, K., Rao, P. K., and Kong, Z., 2016, "An Online Sparse Estimation-Based Classification Approach for Real-Time Monitoring in Advanced Manufacturing Processes From Heterogeneous Sensor Data," IIE Trans., **48**(7), pp. 579–598.
[34] Xu, W., Shen, Y., Bergmann, N., and Hu, W., 2016, "Sensor-Assisted Face Recognition System on Smart Glass via Multi-View Sparse Representation Classification," Proceedings of the IEEE 15th International Conference on Information Processing in Sensor Networks, Vienna, Austria, Apr. 11–14, IEEE Press, p. 2.
[35] Xu, W., Lan, G., Lin, Q., Khalifa, S., Bergmann, N., Hassan, M., and Hu, W., 2017, "Keh-Gait: Towards a Mobile Healthcare User Authentication System by Kinetic Energy Harvesting," Proceedings of 24th Annual NDSS Symposium, San Diego, CA, Feb. 26–Mar. 1, pp. 1–15.
[36] Yang, Y., and Nagarajaiah, S., 2014, "Structural Damage Identification via a Combination of Blind Feature Extraction and Sparse Representation Classification," Mech. Syst. Sig. Process., **45**(1), pp. 1–23.
[37] Tootooni, M. S., Fan, M., Sivasubramony, R. S., Rao, P., Chou, C.-A., and Miskovic, V., 2016, "Graph Theoretic Compressive Sensing Approach for Classification of Global Neurophysiological States From Electroencephalography (EEG) Signals," Proceedings of 2016 International Conference on Brain Informatics & Health, Omaha, NE, Oct. 13–16, pp. 42–51.
[38] Tootooni, M. S., Dsouza, A., Donovan, R., Rao, P. K., Kong, Z. J., and Borgesen, P., 2017, "Classifying the Dimensional Variation in Additive Manufactured Parts From Laser-Scanned 3D Point Cloud Data Using Machine Learning Approaches," ASME J. Manuf. Sci. Eng., **139**(9), p. 091005.
[39] Pereda, E., Quiroga, R. Q., and Bhattacharya, J., 2005, "Nonlinear Multivariate Analysis of Neurophysiological Signals," Prog. Neurobiol., **77**(1), pp. 1–37.
[40] Siegel, M., Donner, T. H., and Engel, A. K., 2012, "Spectral Fingerprints of Large-Scale Neuronal Interactions," Nat. Rev. Neurosci., **13**(2), pp. 121–134.
[41] Tu, J. V., 1996, "Advantages and Disadvantages of Using Artificial Neural Networks Versus Logistic Regression for Predicting Medical Outcomes," J. Clin. Epidemiol., **49**(11), pp. 1225–1231.
[42] Wang, Z., and Srinivasan, R. S., 2017, "A Review of Artificial Intelligence Based Building Energy Use Prediction: Contrasting the Capabilities of Single and Ensemble Prediction Models," Renewable Sustainable Energy Rev., **75**(9), pp. 796–808.
[43] Kiang, M. Y., 2003, "A Comparative Assessment of Classification Methods," Decis. Support Syst., **35**(4), pp. 441–454.
[44] Swain, P. H., and Hauska, H., 1977, "The Decision Tree Classifier: Design and Potential," IEEE Trans. Geosci. Electr., **15**(3), pp. 142–147.
[45] Podgorelec, V., Kokol, P., Stiglic, B., and Rozman, I., 2002, "Decision Trees: An Overview and Their Use in Medicine," J. Med. Syst., **26**(5), pp. 445–463.
[46] Jadhav, S. D., and Channe, H., 2016, "Comparative Study of kNN, Naive Bayes and Decision Tree Classification Techniques," Int. J. Sci. Res. (IJSR), **5**(1), pp. 1842–1845.
[47] Westreich, D., Lessler, J., and Funk, M. J., 2010, "Propensity Score Estimation: Neural Networks, Support Vector Machines, Decision Trees (CART), and

Meta-Classifiers as Alternatives to Logistic Regression," J. Clin. Epidemiol., **63**(8), pp. 826–833.
[48] Gonzalez, R. C., and Woods, R. E., 2008, *Digital Image Processing*, Prentice Hall, Upper Saddle River, NJ.
[49] Ben-Haim, Z., and Eldar, Y. C., 2011, "Near-Oracle Performance of Greedy Block-Sparse Estimation Techniques From Noisy Measurements," IEEE J. Sel. Top. Sig. Process., **5**(5), pp. 1032–1047.
[50] Rigollet, P., and Tsybakov, A. B., 2012, "Sparse Estimation by Exponential Weighting," Statist. Sci., **27**(4), pp. 558–575.
[51] Rojas, C. R., and Hjalmarsson, H., 2011, "Sparse Estimation Based on a Validation Criterion," Proceedings of 50th IEEE Decision and Control and European Control Conference (CDC-ECC), Orlando, FL, Dec. 12–15, pp. 2825–2830.
[52] Candes, E., and Tao, T., 2007, "The Dantzig Selector: Statistical Estimation When p is Much Larger Than n," Ann. Stat., **35**(6), pp. 2313–2351.
[53] Chen, S. S., Donoho, D. L., and Saunders, M. A., 2001, "Atomic Decomposition by Basis Pursuit," SIAM Rev., **43**(1), pp. 129–159.
[54] Li, C., Yin, W., Jiang, H., and Zhang, Y., 2013, "An Efficient Augmented Lagrangian Method With Applications to Total Variation Minimization," Comput. Optim. Appl., **56**(3), pp. 507–530.
[55] Tibshirani, R., 1996, "Regression Shrinkage and Selection via the LASSO," J. R. Statist. Soc. B, **58**(1), pp. 267–288.
[56] Donoho, D. L., Tsaig, Y., Drori, I., and Starck, J.-L., 2012, "Sparse Solution of Underdetermined Systems of Linear Equations by Stagewise Orthogonal Matching Pursuit," IEEE Trans. Inf. Theory, **58**(2), pp. 1094–1121.
[57] Efron, B., Hastie, T., Johnstone, I., and Tibshirani, R., 2004, "Least Angle Regression," Ann. Stat., **32**(2), pp. 407–499.
[58] Pati, Y. C., Rezaiifar, R., and Krishnaprasad, P. S., 1993, "Orthogonal Matching Pursuit: Recursive Function Approximation with Applications to Wavelet Decomposition," Proceedings of 27th Asilomar Conference on Signals, Systems and Computers, Pacific Grove, CA, Nov. 1–3, pp. 40–44.
[59] Tipping, M. E., 2001, "Sparse Bayesian Learning and the Relevance Vector Machine," J. Mach. Learn. Res., **1**, pp. 211–244.
[60] Tipping, M. E., and Faul, A. C., 2003, "Fast Marginal Likelihood Maximisation for Sparse Bayesian Models," Proceedings of the 9th International Workshop on Artificial Intelligence and Statistics, Key West, FL, Jan. 3–6, pp. 3–6.
[61] Wipf, D. P., and Rao, B. D., 2004, "Sparse Bayesian Learning for Basis Selection," IEEE Trans. Signal Process., **52**(8), pp. 2153–2164.
[62] Fu, W. J., 1998, "Penalized Regressions: The Bridge Versus the LASSO," J. Comput. Graph. Stat., **7**(3), pp. 397–416.
[63] Wu, T. T., and Lange, K., 2008, "Coordinate Descent Algorithms for LASSO Penalized Regression," Ann. Appl. Stat., **2**(1), pp. 224–244.
[64] Boyd, S., Parikh, N., Chu, E., Peleato, B., and Eckstein, J., 2011, "Distributed Optimization and Statistical Learning via the Alternating Direction Method of Multipliers," Found. Trends® Mach. Learn., **3**(1), pp. 1–122.
[65] Dai, W., and Milenkovic, O., 2009, "Subspace Pursuit for Compressive Sensing Signal Reconstruction," IEEE Trans. Inf. Theory, **55**(5), pp. 2230–2249.
[66] Needell, D., and Tropp, J. A., 2010, "CoSaMP: Iterative Signal Recovery From Incomplete and Inaccurate Samples," Appl. Comput. Harmon. Anal., **26**(3), pp. 301–321.
[67] Bastani, K., Barazandeh, B., and Kong, Z. J., 2018, "Fault Diagnosis in Multistation Assembly Systems Using Spatially Correlated Bayesian Learning Algorithm," ASME J. Manuf. Sci. Eng., **140**(3), p. 031003.
[68] Zou, H., and Hastie, T., 2005, "Regularization and Variable Selection via the Elastic Net," J. R. Statist. Soc. B, **67**(2), pp. 301–320.
[69] Marquaridt, D. W., 1970, "Generalized Inverses, Ridge Regression, Biased Linear Estimation, and Nonlinear Estimation," Technometrics, **12**(3), pp. 591–612.
[70] Ping-Sing, T., and Shah, M., 1994, "Shape From Shading Using Linear Approximation," Image Vision Comput., **12**(8), pp. 487–498.
[71] Fawcett, T., 2006, "An Introduction to ROC Analysis," Pattern Recognit. Lett., **27**(8), pp. 861–874.
[72] Powers, D. M., 2011, "Evaluation: From Precision, Recall and F-Measure to ROC, Informedness, Markedness and Correlation," J. Mach. Learn. Technol., **2**(1), pp. 37–63.
[73] Hagan, M. T., Demuth, H. B., Beale, M. H., and De Jesús, O., 2014, *Neural Network Design*, 2nd ed., PWS Publishing Co., Boston, MA.
[74] Breiman, L., Friedman, J., Stone, C. J., and Olshen, R. A., 1984, *Classification and Regression Trees*, CRC Press, Boca Raton, FL.
[75] Fisher, R. A., 1936, "The Use of Multiple Measurements in Taxonomic Problems," Ann. Human Genet., **7**(2), pp. 179–188.
[76] Hastie, T., Tibshirani, R., and Friedman, J., 2008, *The Elements of Statistical Learning*, Springer-Verlag, New York, NY.
[77] Manning, C. D., Raghavan, P., and Schütze, M., 2008, *Introduction to Information Retrieval*, Cambridge University Press, New York, NY.
[78] Mitchell, T. M., 1997, *Machine Learning*, MIT Press and McGraw-Hill, Burr Ridge, IL.
[79] Allwein, E. L., Schapire, R. E., and Singer, Y., 2000, "Reducing Multiclass to Binary: A Unifying Approach for Margin Classifiers," J. Mach. Learn. Res., **1**, pp. 113–141.
[80] Escalera, S., Pujol, O., and Radeva, P., 2009, "Separability of Ternary Codes for Sparse Designs of Error-Correcting Output Codes," Pattern Recognit. Lett., **30**(3), pp. 285–297.
[81] Escalera, S., Pujol, O., and Radeva, P., 2010, "On the Decoding Process in Ternary Error-Correcting Output Codes," IEEE Trans. Pattern Anal. Mach. Intell., **32**(1), pp. 120–134.
[82] Fürnkranz, J., 2002, "Round Robin Classification," J. Mach. Learn. Res., **2**(Mar), pp. 721–747.
[83] Li, Y., Mohan, K., Sun, H., and Jin, R., 2017, "Ensemble Modeling of *In Situ* Features for Printed Electronics Manufacturing With *In Situ* Process Control Potential," IEEE Robot. Autom. Lett., **2**(4), pp. 1864–1870.
[84] Zhou, Z.-H., 2012, *Ensemble Methods: Foundations and Algorithms*, Chapman & Hall/CRC Press, Boca Raton, FL.
[85] Lombardi, J. P., Salary, R. R., Weerawarne, D. L., Rao, P. K., and Poliks, M. D., 2019, "Image-Based Closed-Loop Control of Aerosol Jet Printing Using Classical Control Methods," ASME J. Manuf. Sci. Eng., **141**(7), p. 071011.
[86] Salary, R., Lombardi, J. P., Weerawarne, D. L., Rao, P. K., and Poliks, M. D., 2018, "A Computational Fluid Dynamics (CFD) Study of Material Transport and Deposition in Aerosol Jet Printing (AJP) Process," ASME 2018 International Mechanical Engineering Congress & Exposition (IMECE 2018), Pittsburgh, PA, Nov. 9–15, Proc. Paper No. 87647.